Resurgent Na+ Current Offers Noise Modulation in Bursting Neurons

Sharmila Venugopal[1]*, **Soju Seki**[1], **David H. Terman**[2], **Antonios Pantazis**[3,4], **Riccardo Olcese**[3], **Martina Wiedau-Pazos**[5], **Scott H. Chandler**[1]

1 Department of Integrative Biology and Physiology, University of California Los Angeles, Los Angeles, CA, United States of America, **2** Department of Mathematics, The Ohio State University, Columbus, OH, United States of America, **3** Department of Anesthesiology & Perioperative Medicine, David Geffen School of Medicine, University of California Los Angeles, Los Angeles, CA, United States of America, **4** Division of Neurobiology, Department of Clinical and Experimental Medicine (IKE) and Wallenberg Center for Molecular Medicine, Linköping University, 581 83 Linköping, Sweden, **5** Department of Neurology, David Geffen School of Medicine, University of California Los Angeles, Los Angeles, CA, United States of America

* vsharmila@g.ucla.edu

Abstract

Neurons utilize bursts of action potentials as an efficient and reliable way to encode information. It is likely that the intrinsic membrane properties of neurons involved in burst generation may also participate in preserving its temporal features. Here we examined the contribution of the persistent and resurgent components of voltage-gated Na+ currents in modulating the burst discharge in sensory neurons. Using mathematical modeling, theory and dynamic-clamp electrophysiology, we show that, distinct from the persistent Na+ component which is important for membrane resonance and burst generation, the resurgent Na+ can help stabilize burst timing features including the duration and intervals. Moreover, such a physiological role for the resurgent Na+ offered noise tolerance and preserved the regularity of burst patterns. Model analysis further predicted a negative feedback loop between the persistent and resurgent gating variables which mediate such gain in burst stability. These results highlight a novel role for the voltage-gated resurgent Na+ component in moderating the entropy of burst-encoded neural information.

Author summary

The nervous system extracts meaningful information from natural environments to guide precise behaviors. Sensory neurons encode and relay such complex peripheral information as electrical events, known as action potentials or spikes. The timing intervals between the spikes carry stimulus-relevant information. Therefore, disruption of spike timing by random perturbations can compromise the nervous system function. In this study we investigated whether the widely-distributed voltage-gated sodium (Na+) ion channels important for spike generation can also serve as noise modulators in sensory neurons. We developed and utilized mathematical models for the different experimentally inseparable components of a complex Na+ channel current. This enabled phenomenological simplification and examination of the individual roles of Na+ components in spike timing control. We further utilized real-time closed-loop experiments to validate model

predictions, and theoretical analysis to explain experimental outcomes. Using such multi-faceted approach, we uncovered a novel role for a resurgent Na^+ component in enhancing the reliability of spike timing and in noise modulation. Furthermore, our simplified model can be utilized in future computational and experimental studies to better understand the pathological consequences of Na^+ channelopathies.

Introduction

Real-time signal detection in uncertain settings is a fundamental problem for information and communication systems. Our nervous system performs the daunting task of extracting meaningful information from natural environments and guides precise behaviors. Sensory neurons for instance use efficient coding schemes such as bursting that aid in information processing [1]. Mathematical models of bursting have helped explain the basic structure of an underlying dynamical system as one in which a slow process dynamically modulates a faster action potential/spike-generating process, leading to stereotypical alternating phases of spiking and quiescence [2, 3]. The so-called *recovery period* of the slow process governs the intervals between bursts which is often susceptible to random perturbations. Uncertainty in spike/burst intervals can alter the timing precision and information in a neural code [4]. Consequently, ionic mechanisms that modulate the recovery of membrane potential during spike/burst intervals, can play a role in maintaining the stability of these timing events and aid neural information processing. Here we examined a candidate mechanism involving neuronal voltage-gated Na^+ currents for a role in the stabilization of burst discharge (durations and intervals) and noise modulation.

Voltage-gated Na^+ currents are essential for spike generation in neurons [5]. The molecular and structural diversity of Na^+ channels and the resultant functional heterogeneity and complexity, suggest their role beyond mere spike generation [6]. For instance, in addition to the fast/transient Na^+ current (I_{NaT}) mediating action potentials, a subthreshold activated persistent Na^+ current (I_{NaP}) participates in the generation of subthreshold membrane oscillations (STO) (e.g., see [7]). These oscillations can lead to membrane resonance by which a neuron produces the largest response to oscillatory inputs of some preferred frequency [8, 9]. Neurons utilize this mechanism to amplify *weak* synaptic inputs at resonant frequencies [10]. The slow inactivation and recovery of I_{NaP} further provides for the slow process required for rhythmic burst generation [11–13] and therefore can contribute to efficient information processing in multiple ways. However, during ongoing activity, random membrane fluctuations can alter the precision and order of burst timings which can distort/diminish the information in neural code. Here, we provide evidence that a frequently observed resurgent Na^+ current (I_{NaR}), often coexistent with I_{NaP} might be a mechanism by which neurons stabilize burst discharge while maintaining its order and entropy. The I_{NaR}, in neurons and other excitable cells is an unconventional Na^+ current which physiologically activates from a *brief* membrane depolarization followed by repolarization, such as during an action potential [11, 14–17]. In the well-studied neuronal Nav1.6-type Na^+ channels, such a macroscopic I_{NaR} is biophysically suggested to occur from an open-channel block/unblock mechanism [18, 19]. Consequently, I_{NaR} is known to mediate depolarizing after-potentials and promote high-frequency spike discharge in neurons [14, 20–24]. Sodium channels containing the Nav1.6 subunits carry all three types of sodium currents and are widely distributed in the central and peripheral neurons and participate in burst generation [14, 25]. Sodium channelopathy involving alteration in I_{NaR} and I_{NaP}, and its association with irregular firing patterns and ectopic bursting in disease (e.g., [26–29]),
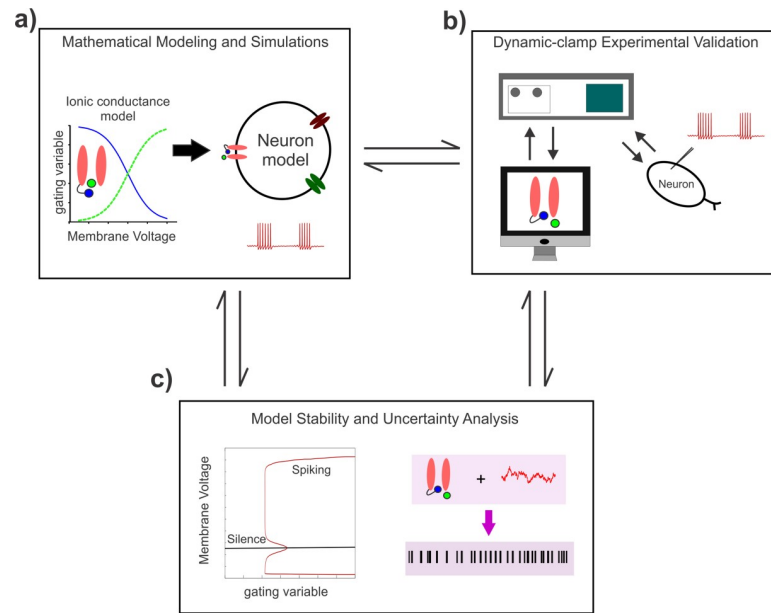
Fig 1. A workflow showing the study components and approaches. a) Development of a mathematical model for the Nav1.6-type Na$^+$ current components and its incorporation into a minimal conductance-based model for a bursting neuron. **b)** Dynamic-clamp validation of model predictions in the brainstem proprioceptive sensory Mes V neurons. **c)** The observed effects on neural discharge are explained using theoretical stability and uncertainty analyses.

prompted us to investigate distinct roles for these Na$^+$ currents in regulating bursting in sensory neurons.

Lack of suitable functional markers and experimental tools to dissociate the molecular mechanism of I_{NaR} from I_{NaP}, led us to use computational modeling and dynamic-clamp electrophysiology to examine a role for I_{NaR} in burst control; however see [19, 23, 24]. Although existing Markovian models model a single channel Nav1.6 type I_{Na} using a kinetic scheme (e.g., [30, 31]), they have limited application for studying exclusive roles of I_{NaR} and I_{NaP} in the control of neural bursting; however see [13, 23, 32, 33]. Here, we developed a novel mathematical model for I_{NaR} using the well-known Hodgkin-Huxley (HH) formalism which closely mimics the unusual voltage-dependent open-channel unblocking mechanism. We integrated the model I_{NaR} into a bursting neuron model with I_{NaP} that we previously reported to study their exclusive roles in burst control in the jaw proprioceptive sensory neurons in the brainstem Mesencephalic V (Mes V) nucleus [8]. To validate model predictions, we used *in vitro* dynamic-clamp electrophysiology, and theoretical stability analysis. Using these approaches, we identify a novel role for I_{NaR} in stabilizing burst discharge and noise modulation in these sensory neurons (see **Fig 1** for a workflow and approaches used).

Results

We first developed a novel HH-based model for the resurgent component of a Nav1.6-type Na$^+$ current and combined it with our previous HH-type models for the transient and persistent Na$^+$ currents [8]. Although the total Na$^+$ current arises from a single channel [11, 30], we formulated the model I_{Na} as a sum of the three components as shown in **Fig 2A** (also see **Methods**): the transient, I_{NaT}, the resurgent, I_{NaR}, and, the persistent, I_{NaP} current. This enabled easy manipulation of individual components to study their exclusive role in burst control. We ensured that each of these components mimic the distinct voltage-dependencies and

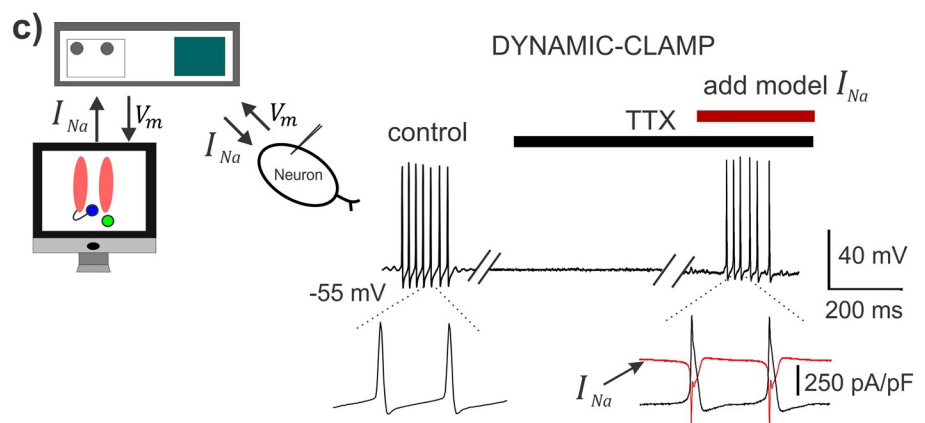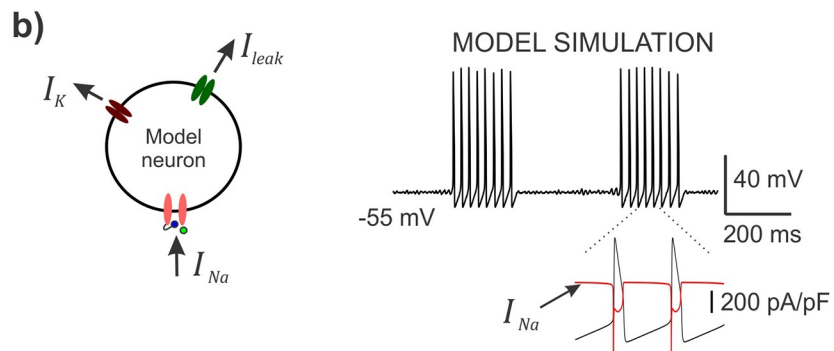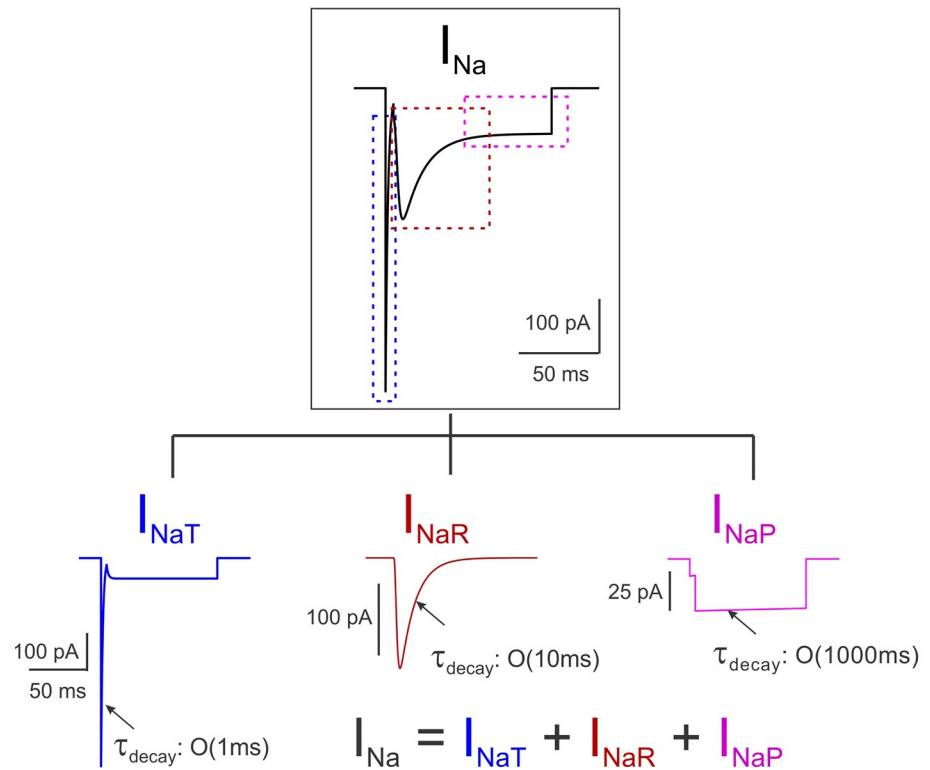**a)** A model for Nav1.6 type sodium currents

$$I_{Na} = I_{NaT} + I_{NaR} + I_{NaP}$$

b)

c)

Fig 2. A Hodgkin-Huxley model for the Nav1.6 Na$^+$ current with the three components. a) A simulated trace showing total I_{Na}; the tree map shows each of the three components: transient I_{NaT}, resurgent I_{NaR}, and, persistent I_{NaP}; These are also highlighted by the color-matched dashed boxes in the top panel. The τ_{decay} shows the order of magnitude of the decay kinetics of the three components. **b)** *Left*: A schematic showing a conductance-based minimal model for a bursting neuron with the I_{Na} incorporated; other ionic currents in the model include a delayed-rectifier potassium (I_K) and a leak current (I_{leak}). *Right*: Model simulation demonstrates rhythmic burst discharge and inset highlights the I_{Na} current in the model during action potentials, in red. **c)** *Left*: Schematic shows the dynamic-clamp experimental approach; V_m is the membrane potential. *Right*: Membrane potential recorded from a rhythmically bursting sensory neuron; action potentials were blocked using 1μM TTX, and dynamic-clamp model I_{Na} was applied to regenerate spikes; double slanted lines indicate break in time; inset highlights the dynamic-clamp I_{Na} in red, during action potentials.

kinetics observed during voltage-clamp recording in Mes V neurons [11, 34]. The classic I_{NaT} with fast inactivation kinetics (order of 1 ms) mediates spike generation, the persistent I_{NaP} with slow inactivation/recovery (order of 1000 ms) mediates STO and provides for the slow process responsible for rhythmic bursting in Mes V neurons [8, 35, 36], and, the resurgent I_{NaR} which mimics the phenomenology of an open channel unblock mechanism with a peak time of ~6 ms and decay kinetics on the order of 10 ms [11, 19, 30] (also see **Fig 3**).

We compared our model I_{Na} and its components to the macroscopic I_{Na} observed in voltage-clamp recordings in Mes V neurons [11, 14] to ensure qualitative and quantitative similarities (see **Fig 3B**). We further ensured that our I_{Na} model closely resembled the I_{Na} generated in Markovian models [30], which follow a kinetic scheme and do not formulate the three components separately (see **S1 Fig**). Our model I_{Na} also satisfied previously described contingency of Nav1.6-type Na$^+$ channels carrying resurgent current: activation of I_{NaR} only up on brief depolarization followed by hyperpolarization to ~ -40 mV, and the correspondence between maximum channel availability and peak time of resurgent current[30] (see **S2 Fig**).

We incorporated the model I_{Na} into a conductance-based single-compartment neuron model (see schematic and membrane voltage trace in black in **Fig 2B**). Together with a minimal set of Na$^+$, K$^+$ and leak conductances, the model neuron faithfully reproduced an expected rhythmic burst discharge observed in Mes V sensory neurons; the total I_{Na} generated during action potentials is shown in expanded time in the figure (red trace). **Fig 2C** shows the dynamic-clamp experiment in an intrinsically bursting Mes V neuron. The control burst was generated by simply driving the neuron with a step depolarization, following which we blocked action potential generation by bath application of tetrodotoxin (1 μM TTX) (see black horizontal bar in **Fig 2C**). Subsequently, we introduced the real-time model I_{Na} using dynamic-clamp during TTX application and by adjusting the conductances of the three I_{Na} components suitably, we were able to regenerate action potential bursts (see **Methods** on the choice of conductance values). The dynamic-clamp I_{Na} generated during action potentials is shown in expanded time in the figure for comparison with the model simulation in **Fig 2B** (red trace).

A novel HH-based mathematical model for resurgent Na$^+$ current

As noted earlier, the total I_{Na} in our model has the novel resurgent component, I_{NaR}; the transient and persistent components are similar to our previous report [8]. **Fig 3A (left panel)** illustrates a well-accepted mechanism of Na$^+$ resurgence [30], wherein a putative blocking particle occludes an open channel following brief depolarization such as during an action potential; subsequently upon repolarization, a voltage dependent unblock results in a resurgent Na$^+$ current. Our I_{NaR} formulation recapitulates this unusual behavior of Na$^+$ channels using nonlinear ordinary differential equations for a blocking variable (b_r) and a competing inactivation (h_r) (see **Methods**). Different from a traditional activation variable of an ionic current in HH models, we formulated the I_{NaR} gating using a term $(1-b_r)$ to enable an unblocking process
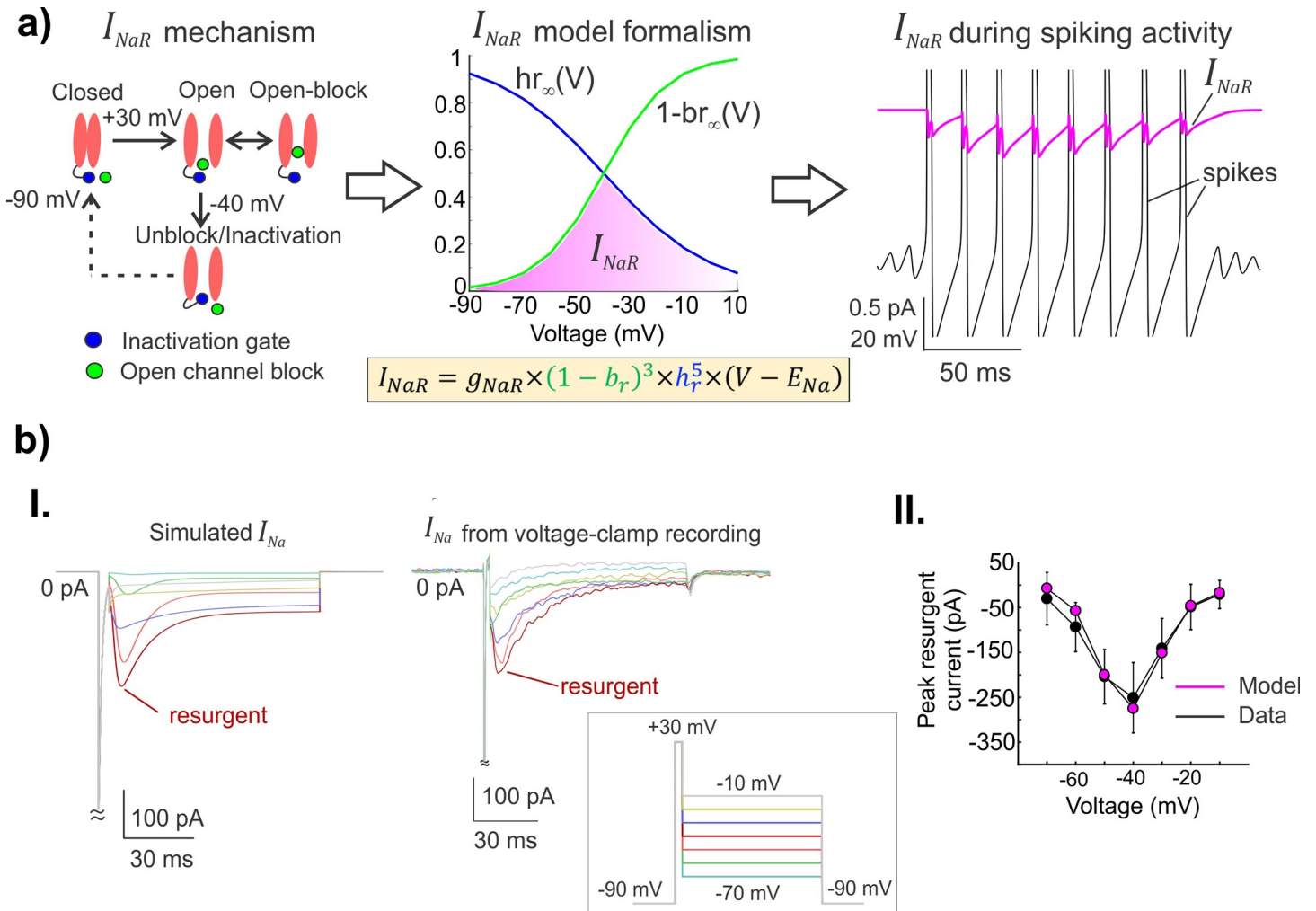
Fig 3. A novel mathematical model for the unusual resurgent component of the Nav1.6-type Na$^+$ current. a) *Left*: A schematic showing the voltage-dependent operation of a Na$^+$ channel mediating resurgent current; open-channel block/unblock (green circle); classic inactivation gate (blue ball and chain). *Middle*: The steady-state voltage-dependencies of open-channel unblocking ($1-br_\infty(V)$) and a competing inactivation process $hr_\infty(V)$ for the novel resurgent component are shown (also see **Methods** and **Results**); the magenta shaded region highlights the voltage range over which I_{NaR} can be observed during open-channel unblocking. The equation for I_{NaR} is shown with novel blocking (b_r), and inactivation (h_r) gating variables. *Right*: The simulated I_{NaR} (in magenta) with peaks occurring during the repolarization phase of action potentials (in black) is shown. **b) I.** A comparison between simulated I_{Na} and experimentally generated I_{Na} from voltage-clamp recording is shown; boxed inset shows the experimental protocol typically used to test for voltage-dependent activation of I_{NaR}. **II.** Graphs show the nonlinear current-voltage relationship of peak resurgent current in the model (magenta) and average peak resurgent currents measured from voltage-clamp experiments (black); error bars show standard deviation (n = 5 neurons from 5 animals).

(see I_{NaR} equation in **Methods** and in **Fig 3A**). Here, the model variable b_r reflects the fraction of channels in the blocked state at any instant, and '1' denotes the maximum proportion of open channels, such that $(1-b_r)$ represented the fraction of unblocking channels. Such a formulation enabled mimicking the open-channel unblocking process as follows: Normally the b_r is maintained 'high' such that $(1-b_r)$ term is small and therefore no I_{NaR} flows, except when a spike occurs, which causes b_r to decay in a voltage-dependent manner. This turns on the I_{NaR} which peaks as the membrane voltage repolarizes to ~ -40 mV, following which the increasing inactivation variable h_r gradually turns off the I_{NaR}. The steady-state voltage dependency of unblock, $(1-br_\infty(V))$, and the competing inactivation ($hr_\infty(V)$) in the model are shown in **Fig 3A (middle panel)**, along with the equation for I_{NaR}; the magenta shaded region highlights the

voltage-dependency of I_{NaR} activation as posited to occur during open-channel unblocking. In **Fig 3A** (**right panel**), we show simulated I_{NaR} (in magenta), peaking during the recovery phase of spikes (in black). In **Fig 3B** (**I.**), we reproduced experimentally observed I_{Na} during voltage-clamp recording and highlight the resurgent component in both model (*left*) and experiment (*right*), (inset shows experimental protocol; also see legend and **Methods**). A comparative current-voltage relationship for the model and experiments is shown in **Fig 3B** (**II.**); also see **S3 Fig** for detailed kinetics of model I_{NaR}. Taken together, the above tests and comparisons ensured the suitability of our model for further investigation of I_{NaR} mediated burst control.

Resurgent and persistent Na$^+$ currents offer push-pull modulation of spike/burst intervals

Given that I_{NaR} is activated during the recovery phase of an action potential, physiologically, any resulting rebound depolarization may control the spike refractory period, and increase spike frequency and burst duration [22, 37]. We tested this by selectively increasing the maximal resurgent conductance g_{NaR} in our model neuron simulation and validated the predictions using dynamic-clamp experiments as shown in **Fig 4A and 4B**. In parallel, we also exclusively modified the maximal persistent conductance g_{NaP} using model simulations and verified the effects using dynamic-clamp experiments as shown in **Fig 4C and 4D**. We only focused on rhythmically bursting Mes V neurons and quantified the burst timing features including the inter-burst intervals (IBIs), burst duration (BD) and inter-spike intervals (ISIs) as illustrated in the boxed inset in **Fig 4**. **Figure panels 4e –j** show a comparison of the exclusive effects of g_{NaR} versus g_{NaP} on each of these burst features. These experimental manipulations using model currents and quantification of resulting burst features revealed significant differences and some similarity between the action of g_{NaR} and g_{NaP} in burst control. First, increases in g_{NaR} resulted in *longer* IBIs, which was in contrast with the effects of the persistent Na$^+$ conductance, g_{NaP}, which *decreased* IBIs (effect highlighted with red double arrows in **Fig 4A–4D** and quantified using box plots in **Fig 4E and 4H**). Alternatively, increasing g_{NaR} *reduced* ISIs, while g_{NaP} had the opposite effect on these events, resulting in an overall *increase* in ISIs with g_{NaP} increases (see **Fig 4F and 4I**); whereas g_{NaR} and g_{NaP} had similar effect in increasing BDs (see **Fig 4G and 4J**). Box plots in **Fig 4E–4J** show 1st, 2nd (median) and 3rd quartiles; error bars show 1.5x deviations from the inter-quartile intervals. For each case (or cell), *n* values represented events (ISI, IBI and BD) and reported here are within-cell effects for different g_{NaR} and g_{NaP} applications during 20 sec step-current stimulation. For the g_{NaR} applications (or series), IBI mean ± std were 210.49 ± 69.33 (control, *n* = 7), 450.29 ± 116.56 (1x, *n* = 26) and 1074.06 ± 199.17 (2x, *n* = 11), and for g_{NaP} applications, these values were 1448.71 ± 450.92 (control, *n* = 4), 910.10 ± 527.27 (1x, *n* = 8) and 644.35 ± 234.19 (1.5x, *n* = 6). For g_{NaR} series, ISI mean ± std were 20.26 ± 1.65 (control, *n* = 59), 12.56 ± 2.25 (1x, *n* = 646) and 10.56 ± 1.81 (2x, *n* = 783), and for g_{NaP} series these values were 12.76 ± 1.13 (control, *n* = 159), 12.57 ± 1.05 (1x, *n* = 611) and 13.56 ± 1.42 (1.5x, *n* = 503). For g_{NaR} series, BD mean ± std were 176.36 ± 69.57 (control, *n* = 8), 300.56 ± 77.90 (1x, *n* = 27) and 671.16 ± 285.96 (2x, *n* = 12), and for g_{NaP} series these values were 346.59 ± 88.39 (control, *n* = 4), 571.30 ± 197.56 (1x, *n* = 8) and 1334.20 ± 592.59 (1.5x, *n* = 7). Treatment effects and group statistics for all the replicates showing the above effects across six Mes V bursting neurons, each from a different animal are summarized in **S2 Table**. A one-way ANOVA was used to test the treatment effects of g_{NaR} and g_{NaP} applications, and when significant, a *post hoc* two-sample Student t-test was used for group comparisons between control and 1x, 1x and 2x, and control and 2x for g_{NaR} cases, and between control and 1x, 1x and 1.5x, and control and 1.5x for g_{NaP} cases. Asterisks above box plots between groups in **Fig 4E–4J** indicate $p < 0.05$ using two-sample Student t-tests for
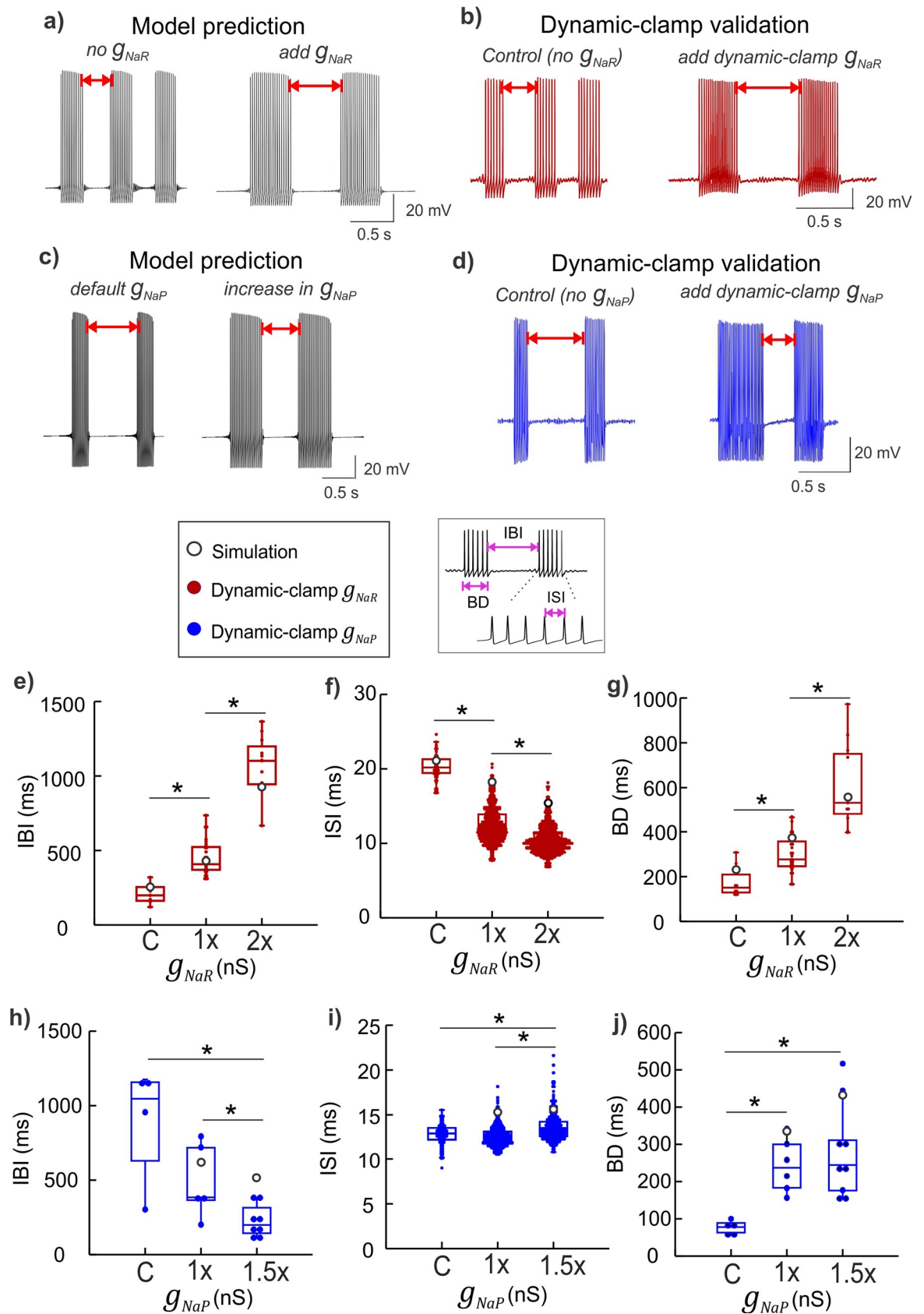
Fig 4. Physiological consequences of I_{NaR} and I_{NaP} on burst discharge. a, c) Simulated membrane voltage demonstrating the effect of g_{NaR} addition **(a)**, and g_{NaP} increase **(c)** on burst discharge. **b, d)** Dynamic-clamp experimental traces showing effects of real-time

addition of g_{NaR} (**b**) and g_{NaP} (**c**) in intrinsically bursting sensory neurons; the red double arrows highlight the opposite effects of increases in g_{NaR} and g_{NaP} on inter-burst intervals in panels (**a–d**). The boxed inset (*left*) indicates color coding of traces for panels **e–j**. The boxed inset (*right*) highlights burst features quantified in panels (**e–j**): inter-burst intervals (IBI), burst duration (BD), and inter-spike intervals (ISI). **e–j**) Box plots showing IBIs (**e, h**), BDs (**f, i**), and ISIs (**g, j**) for application of a series of g_{NaR} or g_{NaP} conductance values (see **Results** for statistics). Model values of 1x g_{NaR} and g_{NaP} are adjusted to match experimental data for 1x application of the corresponding conductance tested; C is control, values of g_{NaR} used for dynamic-clamp are 2 and 4 nS/pF for 1x and 2x respectively, and, values of g_{NaP} used are 0.25 and 0.375 nS/pF for 1x and 1.5x respectively. Asterisks indicate a $p < 0.05$ using a Student t-Test for group comparisons.

post-hoc comparisons. Furthermore, as shown in **Fig 4**, the model simulations predicted consistent effects (note white circles denote predicted values in panels **e—j**) with dynamic-clamp experiments, making the model suitable for further analysis of I_{NaR}/I_{NaP} mediated mechanism of burst control (see *white circles* in panels **4e** - **j**). In two additional bursting neurons, we also conducted g_{NaR} and g_{NaP} subtraction experiments which showed consistent reverse effects of additions (see **S4 Fig and legend**). In the g_{NaP} subtraction experiment, note that a -2x g_{NaP} resulted in the abolition of bursting and subthreshold oscillations as shown in the figure. Such an effect was reproduced in the neuron model by setting g_{NaP} = 0, as shown in **S4C Fig**.

To test whether I_{NaR} and I_{NaP} differentially modulate the regularity and precision of spike timing we observed the inter-event intervals (or IEIs) during real-time addition of g_{NaR} and g_{NaP}. As shown in **Fig 5A and 5B**, addition of g_{NaR} improved the regularity of the two types of events: the longer IBIs and the shorter ISIs, whereas, addition of g_{NaP} did not show such an effect. Note that application of real-time g_{NaR} improved both the timing precision and regularity of IBIs (compare *left* and *right* panels of **Fig 5A**), while application of dynamic-clamp g_{NaP} did not seem to affect either of these features (compare *left* and *right* panels of **Fig 5B**). Furthermore, in **Fig 5C** we highlight that g_{NaR} application also improved spike-to-spike regularity of ISIs within bursts (shown are two representative bursts for g_{NaR} (**Fig 5C**, *left* panel) versus g_{NaP} (**Fig 5C**, *right* panel) application from **Fig 5A and 5B** (see figure legend). Taken together, these opposite effects of persistent and resurgent Na$^+$ currents arising from a single Na$^+$ channel may act in concert to offer a *push-pull* modulation of burst timing regulation.

Resurgent Na$^+$ aids stabilization of burst discharge

The effect of persistent g_{NaP} in reducing IBIs can be explained by its subthreshold activation [11], wherein increases in g_{NaP} *promotes* STO and burst initiation which in turn increases burst frequency and reduces IBIs. Additionally, a high g_{NaP} together with its slow inactivation helps maintain depolarization which can increase BDs. During spiking, I_{NaP} inactivation slowly accumulates and can contribute to any spike frequency adaptation as a burst terminates. Further increases in g_{NaP} can accentuate such an effect and lead to increases in spike intervals within a burst. In contrast, the rebound depolarization produced due to I_{NaR} can decrease ISIs and promote spiking which prolongs the BDs. An effect which is not immediately obvious is an increase in IBI due to increases in g_{NaR} since IBIs are order of magnitude slower events than rise/decay kinetics of I_{NaR}. Moreover, this current is not active during IBIs. It is likely that I_{NaR} which promotes spike generation produces its effect on lengthening the IBIs by further accumulation of I_{NaP} inactivation during spiking and in turn reducing channel availability immediately following a burst. We examined this possibility using model analysis of I_{NaR}'s effect on modulating the slow I_{NaP} inactivation/recovery variable, h_p.

The simulated membrane potential (grey traces) and the slow I_{NaP} inactivation/recovery variable, h_p (overlaid magenta traces) of the model neuron under three conditions shown in **Fig 6A–6C**: 1) with default values of g_{NaR} and g_{NaP} (**Fig 6A**), 2) an 1.5x increase in g_{NaP} (**Fig 6B**), and, 3) a 2x increase in g_{NaR} (**Fig 6C**). The peak and trough of the slow inactivation/
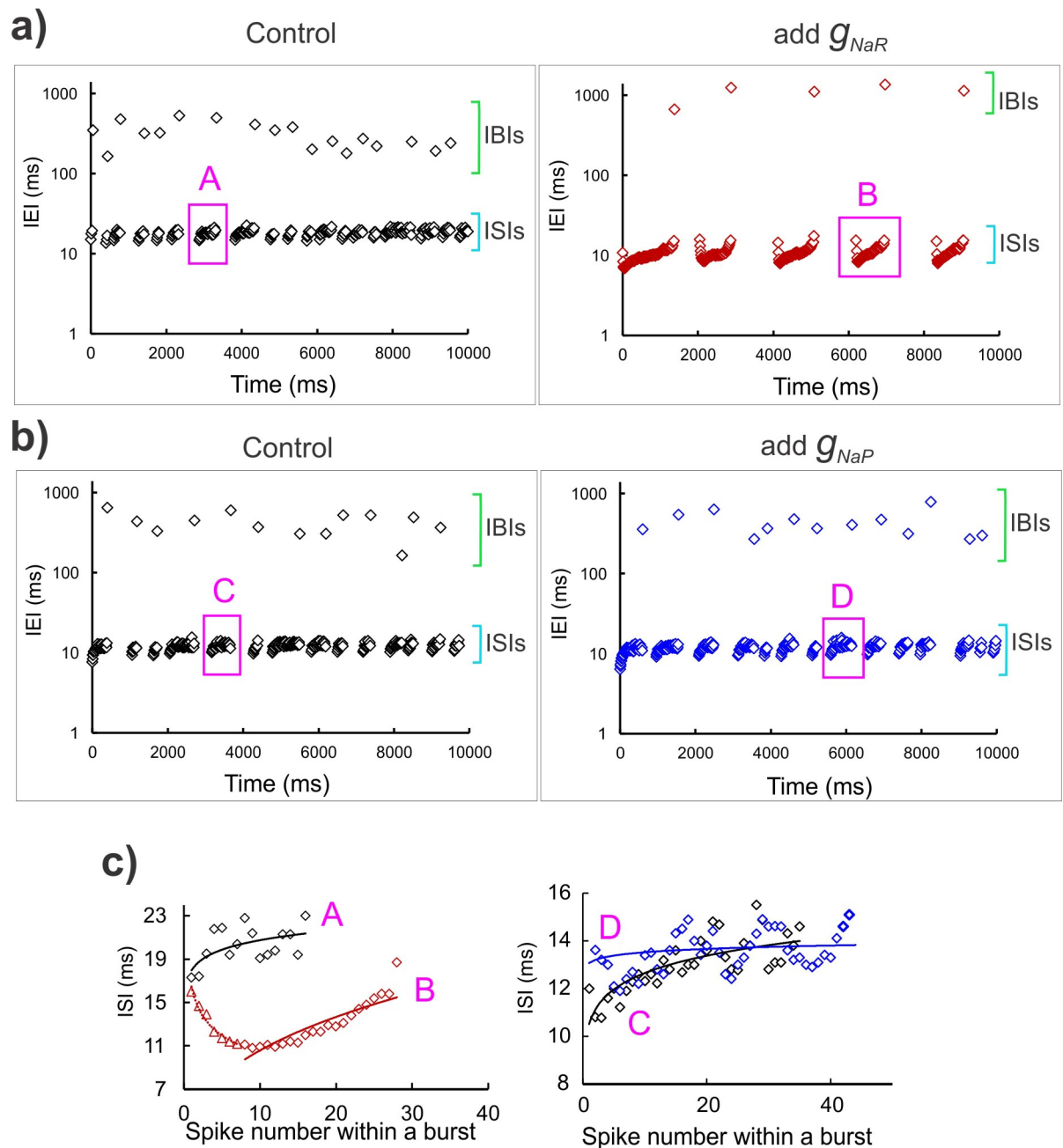
Fig 5. Spike timing regularity monitored by I_{NaR}. a, b) Time series graphs showing inter-event intervals (IEIs) under control condition (*left panels* in both **a, b**), and dynamic-clamp addition of g_{NaR} (*right panel* in **a**), and g_{NaP} (*right panel* in **b**). The green and cyan square brackets in each panel highlight the IBI and ISI range respectively. The y-axis shows IEIs on a log scale. Magenta boxes demarcate a representative burst in each case, which is expanded in the graphs in **c)**, corresponding with the bold letters, A, B, C and D. The solid lines in (**c**) are power regression fit in each case; in all the panels, black open diamonds are control, maroon open diamonds correspond with g_{NaR} application and blue open diamonds correspond with the g_{NaP} application.

recovery variable, h_p correspond to burst *onset* and *offset* respectively. Comparing these traces in the three panels, we note that an increase in g_{NaR} effectively lowers the h_p value at which burst terminates (see curvy arrow in **Fig 6C** and legend). This observation was further supported by estimations of theoretical thresholds for *burst onset* and *offset* for increasing values of g_{NaR} (**Fig 6D**) and, similar thresholds for increasing values of g_{NaP} are provided for
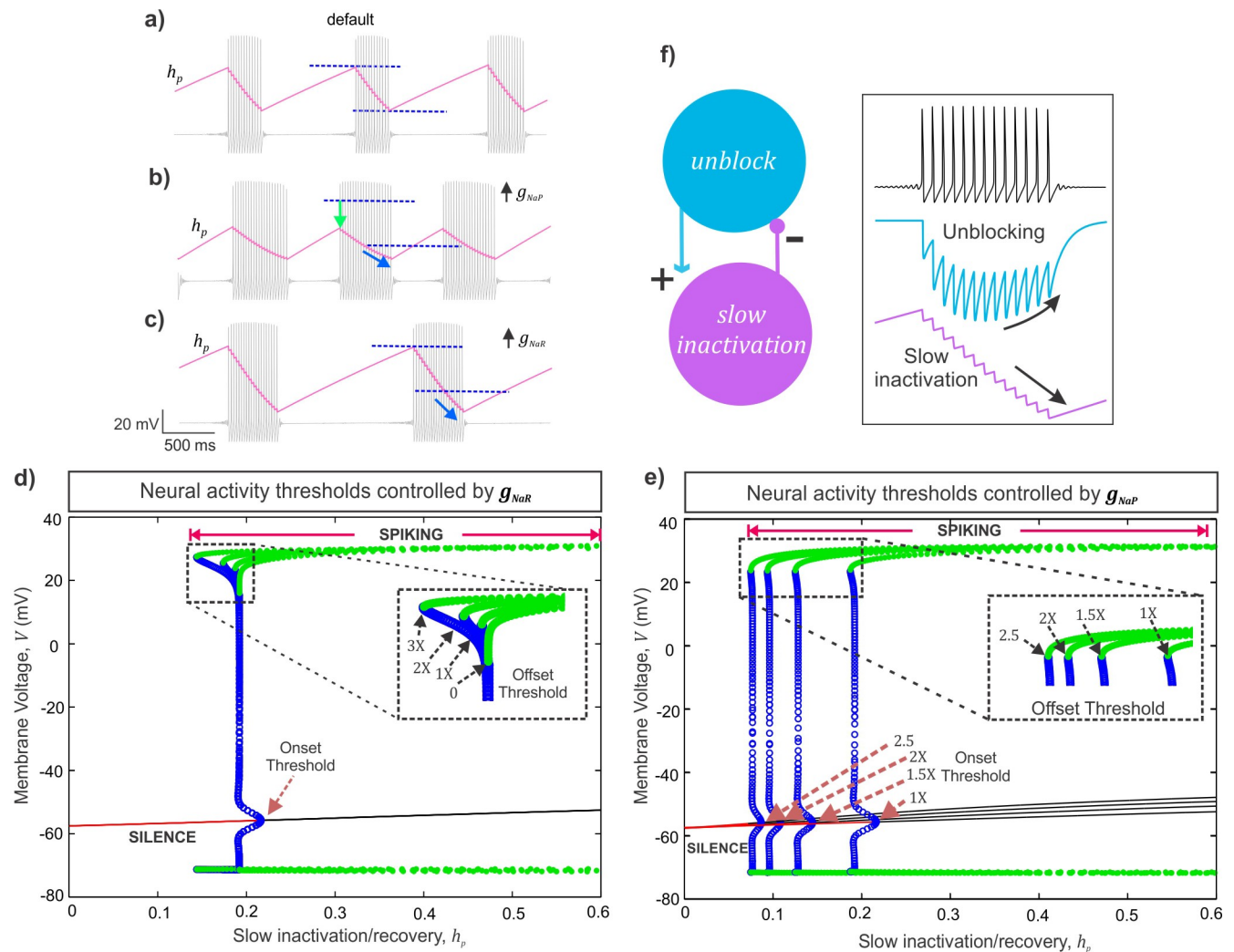
Fig 6. Analysis of a mechanism of action of I_{NaR} and I_{NaP}. a-c) The slow I_{NaP} inactivation/recovery variable, h_P is overlaid (magenta) on membrane voltage traces (grey) under default (**a**), 1.5x g_{NaP} (**b**), and 2x g_{NaR} (**c**) conditions; the dark blue dashed lines in (**a-c**) indicate the maximum and minimum values of the persistent inactivation variable under default condition; the light green arrow in (**b**), highlights a reduced peak recovery required for burst onset; the light blue curvy arrows in (**b, c**) indicate further accumulation of slow inactivation before burst termination. **d, e)** Bifurcation diagrams showing the steady states and spiking regimes of the membrane voltage (V) and slow I_{NaP} inactivation/recovery (h_p). The red solid lines represent resting/quiescence states consistent with low values of h_p. The meeting points of stable equilibria (red) and unstable equilibria (black solid lines) represents the theoretical threshold for burst onset, the Hopf bifurcation point (see **S1 Text**). The blue open circles are the unstable periodics that form region of attraction on either side of the stable equilibria for sub-threshold membrane voltage oscillations; the meeting point of the curve of unstable periodics with the stable periodics (green filled circles) represents the theoretical threshold for burst offset/termination, saddle node of periodics (see **S1 Text**). The dashed boxes in (**d**) and (**e**) magnify the burst offset thresholds due to increases in g_{NaR} (**d**) and g_{NaP} (**e**); brown dashed arrows in (**e**) highlight shifts in burst onset thresholds due to g_{NaP} increases; 1X g_{NaR} = 3.3 nS/pF and 1X g_{NaP} = 0.5 nS/pF. **f)** Schematic showing a negative feedback loop between the unblocking process and the slow inactivation of the Na$^+$ currents. Inset shows membrane potential (top), blocking variable, b_r (middle) and slow inactivation, h_r (bottom), illustrating the negative feedback mechanism.

comparison in **Fig 6E** (see legend and **S1 Text** for details). Note that changes in g_{NaR} did not alter the burst onset thresholds, consistent with a lack of resurgent current before spike onset (see brown arrow indicating burst onset threshold in **Fig 6D**). In contrast, increasing g_{NaR}, consistently *lowered* the threshold values of slow inactivation/recovery for burst offset (see highlighted dashed box with arrows pointing to the burst offset thresholds decreasing with increasing g_{NaR} values in **Fig 6D**). The net effect is longer recovery time between bursts and therefore prolonged IBIs. Additionally, in **Fig 6D**, an increase in g_{NaR} extended the range of slow

inactivation/recovery for which stable spiking regime exists (marked by the green circles). This *gain in stability* is indicative of a *negative feedback loop* in the Na$^+$ current gating variables which model the slow inactivation and the open-channel unblock process. As shown in **Fig 6F** (see boxed inset), during a burst, presence of a channel unblocking process and the resulting resurgent Na$^+$ can lead to further accumulation of slow inactivation (a positive effect) which eventually shuts off the unblocking events with further inactivation (negative feedback), and terminates a burst. The schematic on the left in **Fig 6F** summarizes a negative feedback loop between the unblocking and slow inactivation processes of Na$^+$ currents which could mediate the stabilization of burst discharge as described above.

Resurgent Na$^+$ current offers noise tolerance

Next, we examined whether the stability of burst discharge offered by the presence of I_{NaR} can also contribute to noise tolerance. During quiescence/recovery periods between bursts, the membrane voltage is vulnerable to perturbations by stochastic influences, which can induce abrupt spikes and therefore disrupt the burst timing precision. We introduced a Gaussian noise to disrupt the rhythmic burst discharge in the model neuron when no g_{NaR} was present as shown in **Fig 7A and 7B**. Subsequent addition of g_{NaR} restored burst regularity (**Fig 7C**). Model analyses in the (h_p,V) plane provides insight into the mechanism of I_{NaR} mediated noise tolerance. Briefly, we project a portion of a (h_p,V) trajectory corresponding to the termination of one burst until the beginning of the next (see expanded insets in **Fig 7A, 7B and 7C**) to the (h_p,V) diagrams shown in **Fig 7D, 7E and 7F** respectively (see **S1 Text** for details). In **Fig 7D**, beginning at the magenta circle, the (h_p,V) trajectory (magenta trace) moves to the right as h_p recovers during an IBI, until a burst onset threshold is crossed; point where the blue circles meet the red and black curves (see **S1 Text** for details), and eventually bursting begins; see upward arrow marking a jump-up in V at the onset of burst. During a burst, while V jumps up and-down during spikes, h_p moves to the left as slow inactivation accumulates during bursting (left arrow). Finally, when h_p reduces sufficiently, (h_p,V) gets closer to the burst offset threshold (points at which the green and blue circles meet), and the burst terminates (down arrow). *What is key in this figure* is that the IBI is well-defined as the time period in which the (h_p,V) trajectory moves along the red curve of steady states during the recovery process and moves past the burst onset threshold until a burst begins. However, when stochastic influences are present, the recovery period near-threshold is subject to random perturbations in V and can cause abrupt jump-up/spikes during the recovery period (see expanded inset in **Fig 7B**). Projecting (h_p,V) during this period on to **Fig 7E**, we note that the near-threshold noise amplitudes can occasionally push the (h_p,V) trajectory (magenta) above a green region of attraction and this results in such abrupt spikes. Now, when g_{NaR} is added, the apparent restoration of burst regularity (see **Fig 7C**) can be attributed to an expansion in this green shaded region as shown in **Fig 7F** (see arrow pointing to a noise-tolerant region). In this situation, near-threshold random perturbations have less of an effect during the recovery process to induce abrupt spikes. *This way, the net effect of I_{NaR} on slow Na$^+$ inactivation prevents abrupt transitions into spiking regime following burst offset and in turn contributes to burst refractoriness and noise tolerance.* We suggest that such a mechanism can make random fluctuations in membrane potential less effective in altering the precision of bursts and therefore aid information processing.

Resurgent Na$^+$ moderates burst entropy

The spike/burst intervals, their timing precision and order are important for information coding [38–42]. Given our prediction that I_{NaR} can offer noise tolerance and stabilize burst discharge, we examined whether it can reduce uncertainty in spike/burst intervals and restore
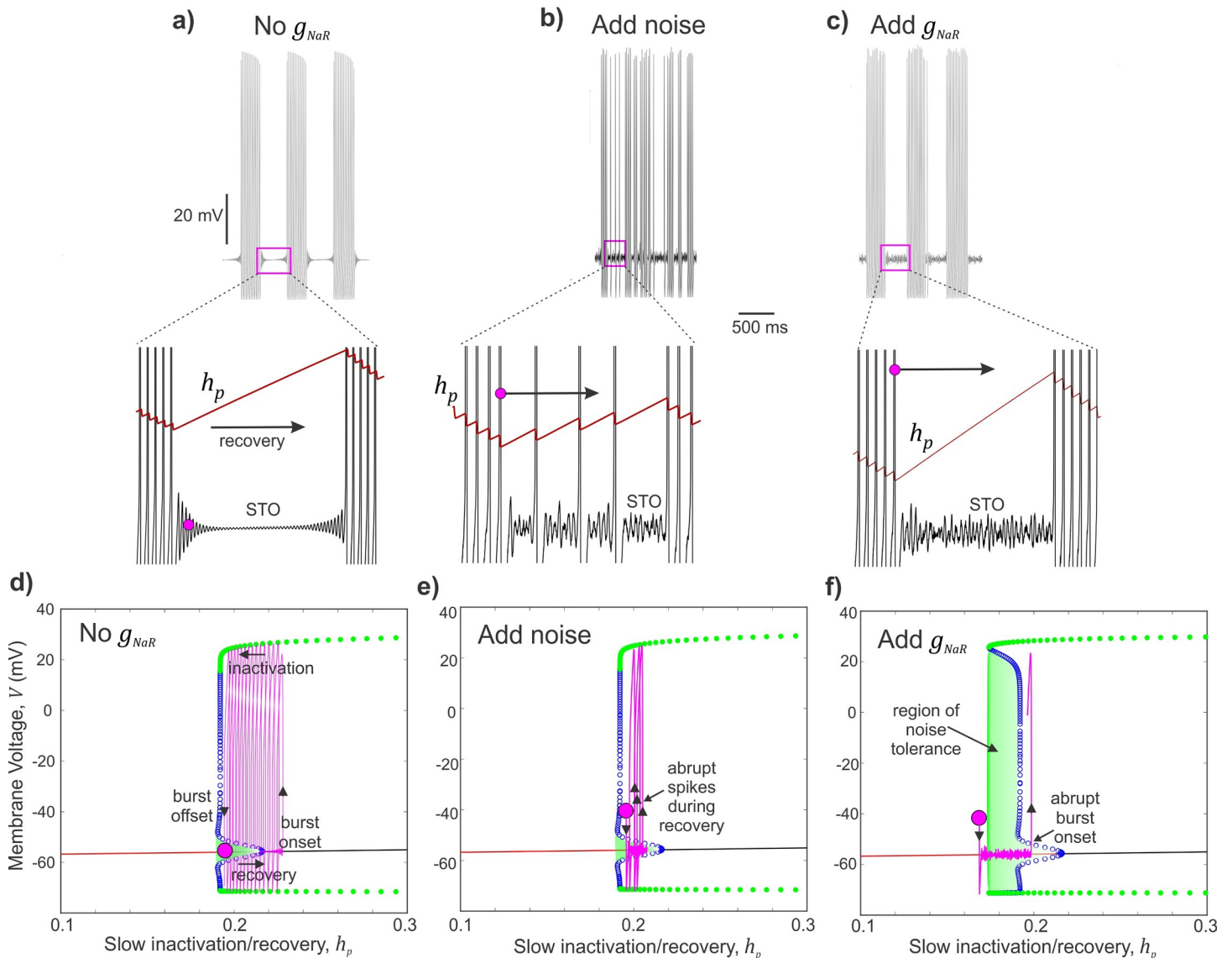
Fig 7. Resurgent Na⁺ current offers burst stability and noise modulation. a—c) Simulated membrane voltage shows neural activity patterns without any g_{NaR} **(a)**, with additive Gaussian noise input **(b)**, and with subsequent addition of g_{NaR} **(c)**. Expanded regions in **(a-c)** show membrane voltage sub-threshold oscillations (STO) during an inter-burst interval. Also overlaid is the evolution of the slow sodium inactivation/recovery variable; arrow indicates recovery during IBI, and magenta circle marks an arbitrary time point used to track these trajectories in **(d—f)**. **d—f)** Bifurcation diagrams with projected trajectories of (h_∞, V), shown in magenta to highlight the effect of addition of noise near sub-threshold voltages **(e)** and then the enlarged region of noise tolerance (highlighted green shaded region) due to addition of g_{NaR} in **(f)**. The magenta circle marks the beginning time points of each trajectory.

order in burst discharge. We tested this using model simulations and dynamic-clamp experiments as shown in **Fig 8A–8D**. In both cases, as shown by spike raster plots in **Fig 8E and 8F**, we disrupted the inter-event intervals (IEIs) by additive White/Wiener noise input while driving rhythmic burst discharge using step depolarization (also see **Methods**). Subsequent addition of g_{NaR} conductance restored the regularity of rhythmic bursting. We used Shannon's entropy as a measure of uncertainty in IEIs and show that increases in entropy due to noise addition was reduced to control levels by subsequent increases in g_{NaR} as shown in **Fig 8G** (see **Methods**). We also quantified the Coefficient of Variation (CV) and noted that adding noise which shortened IBIs, indeed decreased the CV, due to a reduction in the standard deviation
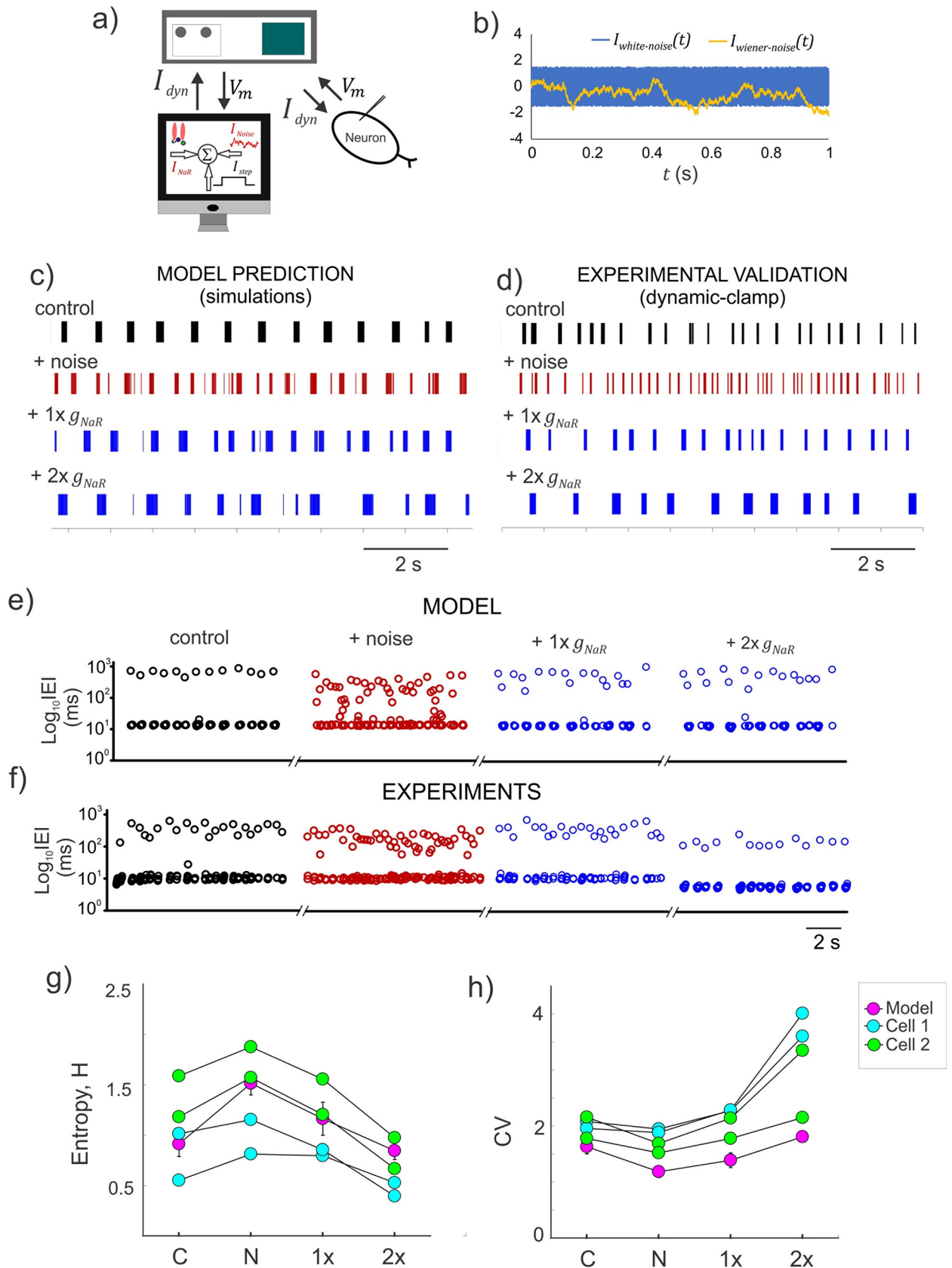
Fig 8. Resurgent Na⁺ current moderates the entropy of burst discharge. a) Schematic showing the experimental setup for real-time application of I_{NaR} and a stochastic input, I_{Noise} (see **Methods**); the dynamic-clamp current, I_{dyn} is the instantaneous sum of I_{NaR}, a step current (I_{step}) and I_{Noise}.

b) Simulated time series of two stochastic noise profiles used to disrupt the rhythmic burst discharge in Mes V neurons; $I_{white-noise}$ was generated from a uniformly distributed random number and $I_{wiener-noise}$ was generated from a normally distributed random number (see **Methods**). **c–d**) Raster plots showing patterns of inter-event intervals (IEIs) for the different conditions shown in the model (**e**), and during dynamic-clamp (**f**). **e–f**) Time series of IEI shown on a log scale for the different conditions shown in the model (**e**), and during dynamic-clamp (**f**). **g–h**) Shannon entropy (H) and coefficient of variability (CV) measured for IEIs under the different conditions presented in (**c**) and (**d**). Plotted circles for the model represent an average across 10 trials, while individual trials are presented for the data points from two cells. In both (**g**) and (**h**), C: control, N: after addition of random noise, 1x and 2x are supplements in g_{NaR} values.

(s.d.) of the IEI distribution. Subsequent addition of I_{NaR}, which significantly lengthened the IBIs, resulted in increases in CV values due to an increase in IEI s.d. Taken together, I_{NaR} moderated burst entropy and improved the regularity of spike/burst intervals.

Discussion

Using a combination of mathematical modeling and simulations, theory and dynamic-clamp electrophysiology, we demonstrate a novel role for voltage-gated Na$^+$ currents in burst control, noise modulation and information processing in sensory neurons. While the subclasses of Na$^+$ currents presented here are experimentally inseparable, our phenomenological simplification using the HH-formalism with *in silico knock-in* of each Na$^+$ current component using dynamic-clamp experiments, allowed examination of their individual contributions to burst control. Additionally, theoretical analysis suggested a putative negative feedback loop between the persistent inactivation and resurgent unblocking processes of the Nav1.6 Na$^+$ channels. These results show the apparent consequences on burst control and signal processing capacity of neurons when these currents are present.

Stabilization of burst discharge by I_{NaR}

In contrast with I_{NaP}, which drives near threshold behavior and burst generation, I_{NaR} facilitated slow channel inactivation as bursts terminate (also note [11]). Increased channel inactivation due to I_{NaR} in turn prolonged the recovery from inactivation required to initiate subsequent burst of activity. Such an interaction between open-channel unblock process underlying I_{NaR}, and, the slow inactivation underlying I_{NaP}, offer a closed-loop *push-pull* modulation of ISIs and IBIs. Specifically, presence of I_{NaR} facilitates slow Na$^+$ inactivation as shown by our theoretical analyses of model behavior; such enhanced slow channel inactivation can eventually shut off channel opening and unblocking. This resulted in burst stabilization. Theoretically, this represented an enlarged separatrix (or boundary) for transitioning from a sub-threshold non-spiking behavior to spiking behavior (see enlarged green shaded region in **Fig 7F**), and the neuron becomes refractory to burst generation and hence offers noise tolerance.

Is this apparent effect of I_{NaR} physiologically plausible? Biophysical studies indicate that recovery from fast inactivation is facilitated in sodium channels that can pass resurgent current [30]; as shown here, this appears to be true for recovery from slow inactivation as well. Consistently, in the SCN8a knockout Med mouse, which lack the Nav 1.6 sodium channel subunit, recordings from mutant cells showed an absence of maintained firing during current injections, limited recovery of sodium channels from inactivation, and failure to accumulate in inactivated states. This is attributed to a significant deficit in I_{NaR} [11, 20, 37]. Furthermore, maintained or repeated depolarization can allow a fraction of sodium channels in many neurons to enter inactivation states from which recovery is much slower than for normal fast inactivation (reviewed in [43]). Here, our simulations and model analyses predict that the presence, and increase in I_{NaR} conductance, provides for a such a physiological mechanism to maintain sustained depolarization and promote fast and slow Na$^+$ inactivation.

Sodium currents and signal processing in neurons

Neuronal voltage-gated Na$^+$ currents are essential for action potential generation and propagation [5]. However, to enable fight-or-flight responses, an overt spike generation mechanism must be combined with *noise modulation* to extract behaviorally relevant inputs from an uncertain input space. Here we show that, the voltage-gated Na$^+$ currents can serve an important role in neural signal processing (see summary in **Fig 9**). As shown in the figure, a sub-threshold activated persistent Na$^+$ current contributes to membrane resonance, a mechanism of bandpass filtering of preferred input frequencies [9]. We call this type of input gating, which is widely known to be important for brain rhythms [9, 41], a *tune-in* mechanism (see figure legend). In some cases ambient noise or synaptic activity can amplify weak inputs and promote burst generation [44, 45]. This way, a tune-in mechanism such as the persistent Na$^+$ current can contribute to weak input detection and promote burst coding [46, 47]. Then again, during rhythmic bursting, presence of resurgent Na$^+$ maintains the order and precision of the timing events of bursts while preventing abrupt transitions into spiking phase due to stochastic influences as shown here. During ongoing sensory processing, such burst timing regulation can provide for noise cancellation or what we call a *tune-out* mechanism, which can mitigate random irregularities encoded in bursts (see **Fig 9** and **legend**). Whether this leads to improved sensory processing in the presence of natural stimuli and/or sensorimotor integration during normal behaviors needs to be validated. Our biological prediction here that a sensory neuron can utilize these voltage-gated Na$^+$ currents as a *tune-in-tune-out* mechanism to gate preferred inputs, attenuate random membrane fluctuations and prevent abrupt transitions into spiking activity supports such a putative role.

Methods

Neuron model for bursting activity

The conductance-based Mes V neuron model that we used to investigate the physiological role for I_{NaR} and I_{NaP} components of I_{Na} in burst discharge, incorporates a minimal set of ionic conductances essential for producing rhythmic bursting and for maintaining cellular excitability in these neurons [8]. These include: 1) a potassium leak current, I_{leak}, 2) sodium current, I_{Na} as described above, and, 3) a 4-AP sensitive delayed-rectifier type potassium current (I_K) [8, 48]. The model equations follow a conductance-based Hodgkin-Huxley formalism [5] and are as follows.

$$V' = (-I_{Na} - I_K - I_{leak} + I_{app})/C$$

$$h'_t = \frac{ht_\infty(V) - h_t}{\tau_t}$$

$$h'_p = \frac{hp_\infty(V) - h_p}{\tau_p(V)}$$

$$b'_r = \alpha_b(1 - b_r)br_\infty(V) - k_b\beta_{br}(V)b_r$$

$$h'_r = \alpha_{hr}(V)hr_\infty(V) - 0.8\beta_{hr}(V)h_r$$

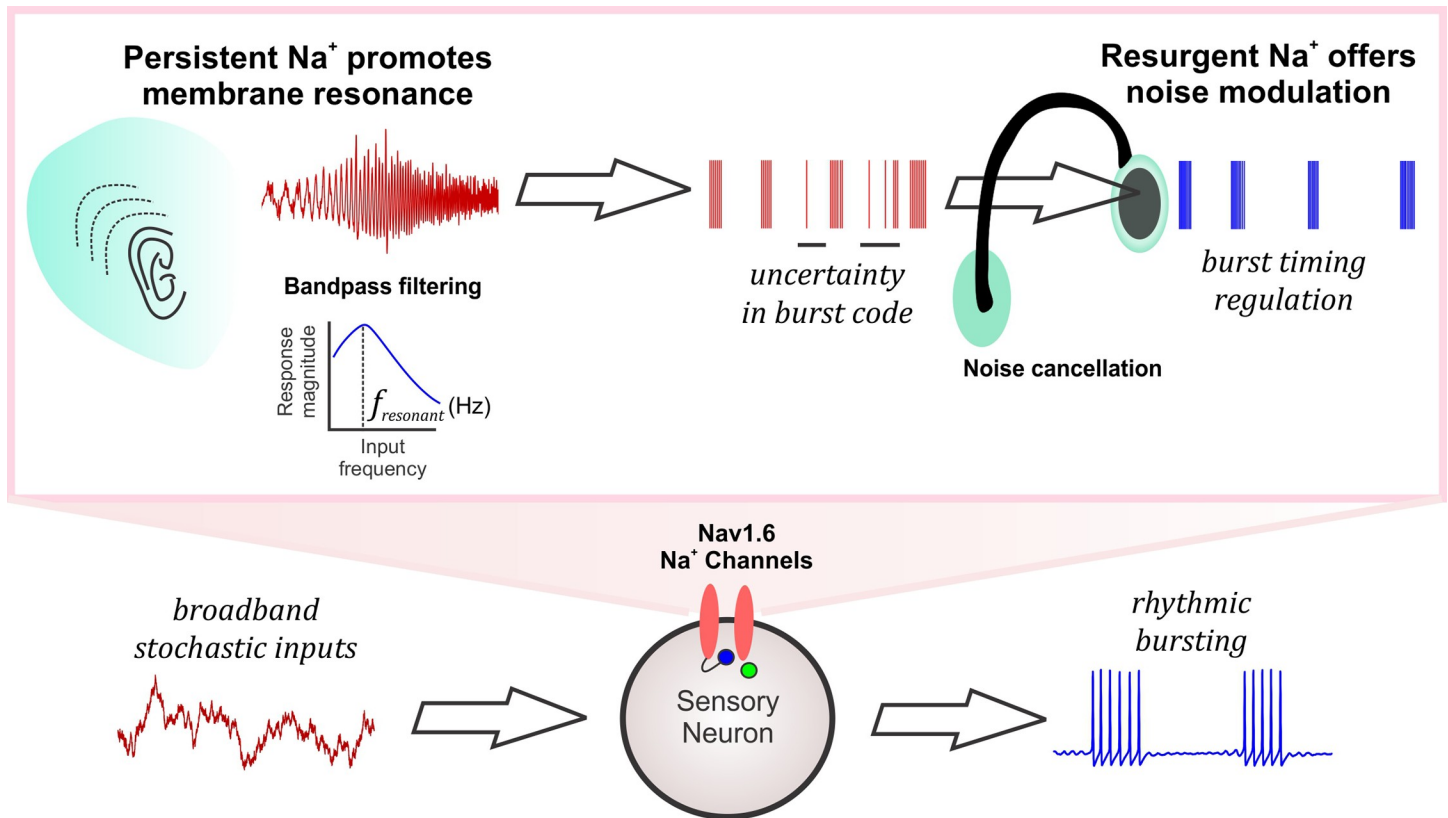$$n' = \frac{n_\infty(V) - n}{\tau_n}$$

Fig 9. A consolidated role for persistent and resurgent Na⁺ currents in information processing. The schematic shows the broadband input space of a sensory neuron which can produce rhythmic bursting activity. The Nav1.6-type Na⁺ channels mediating the persistent Na⁺ current (schematized as a listening ear) enhance neuronal resonance and tune in relevant input frequencies by bandpass filtering ($f_{resonant}$ refers to the resonant frequency of the neuron). Such selected inputs carrying behaviorally relevant stimuli are encoded as bursts but may be prone to uncertainty due to intrinsic or extrinsic stochastic influences. The resurgent Na⁺ current mediated by the Nav1.6 Na⁺ channels improve the regularity of spike/burst timing by mitigating the effects of noise by tuning out random spikes between bursts (schematized as a noise cancelling headphone), thus aiding in neural signal processing.

https://doi.org/10.1371/journal.pcbi.1007154.g009

In what follows, we provide the formulation for each of the ionic currents and describe in detail, the novel I_{NaR} model.

Voltage-gated sodium currents

In vitro action potential clamp studies in normal mouse Mes V neurons, and voltage-clamp studies in Nav1.6 subunit SCN8a knockout mice have demonstrated existence of three functional forms of the total sodium current, I_{Na}, including the transient (I_{NaT}), persistent (I_{NaP}) and resurgent (I_{NaR}) components [11, 14]. Each of these currents is critical for Mes V electrogenesis including burst discharge, however, their exclusive role is yet unclear. Lack of suitable experimental model or manipulation to isolate each of these TTX-sensitive components, led us to pursue an alternative approach involving computational model development of the physiological I_{Na}. To further allow model-based experimental manipulation of individual components of the I_{Na}, we designed a conductance-based model as follows. Although a single Nav1.6 channel can produce all three I_{Na} components observed experimentally, we used a set of three HH-type conductances, one for each of the transient, the persistent, and the resurgent components. This allowed us to easily manipulate these components independently to test their

specific role in neural burst control. The equation for the total sodium current can be written as:

$$I_{Na} = I_{NaT} + I_{NaR} + I_{NaP}$$

where,

$$I_{NaT} = \boldsymbol{g_{NaT}}(m_{t\infty}(V)h_t)(V - E_{Na})$$

$$I_{NaR} = \boldsymbol{g_{NaR}}((1 - b_r)^3 h_r^5)(V - E_{Na})$$

$$I_{NaP} = \boldsymbol{g_{NaP}}(m_{p\infty}(V)h_P)(V - E_{Na})$$

The maximal persistent conductance, g_{NaP} was set 5–10% of the transient, g_{NaT} [49] and the resurgent was set to 15–30% of g_{NaT}, based on the relative percentage of maximum I_{NaR} and I_{NaT} as revealed by voltage-clamp experiments shown in **Fig 3**; E_{Na} is the Na$^+$ reversal potential.

Based on experimental data, the gating function/variable, $m_{t\infty}(V)$, and h_t, for I_{NaT}, and, $m_{p\infty}(V)$, and, h_P, for I_{NaP} are modeled as described in [8]. The rate equations for the inactivation gating variables h_t, and, h_P, model the fast and slow inactivation of the transient and persistent components respectively. The activation gates are steady-state voltage-dependent functions, consistent with fast voltage-dependent activation of I_{Na}.

Steady-state voltage-dependent activation and inactivation functions of *transient* sodium current respectively include:

$$mt_\infty(V) = \frac{1}{1 + e^{\left(-(V+35)/4.3\right)}}; \quad ht_\infty(V) = \frac{1}{1 + e^{\left((V+55)/7.1\right)}}$$

Steady-state activation, inactivation and steady-state voltage-dependent time constant of inactivation for *persistent* sodium current respectively include:

$$mp_\infty(V) = \frac{1}{1 + e^{\left(-(V+50)/6.4\right)}}; \quad hp_\infty(V) = \frac{1}{1 + e^{\left((V+52)/14\right)}}; \quad \tau_p(V) = 100 + \frac{10000}{1 + e^{\left((V+60)/10\right)}}$$

The novel I_{NaR} formulation encapsulates the block/unblock mechanism using a block/unblock variable (b_r), and, a second hypothetical variable for a competing inactivation, which we call, h_r. We call this a *hybrid* model, to highlight the fact that the model implicitly incorporates the history or state-dependent sodium resurgence, following a transient channel opening, and combines this into a traditional Hodgkin-Huxley type conductance-based formulation. In the b_r' and h_r' rate equations for b_r, and, h_r, the block/unblock variable, b_r increases or grows according to the term, $\alpha_b(1-b_r)br_\infty(V)$, and decays as per the term, $k_b\beta_{br}(V)b_r$, described as follows:

$\boldsymbol{\alpha_b(1-b_r)br_\infty(V)}$: In this growth term, we incorporate state-dependent increase in b_r, as follows; we assume that the rate of increase in b_r is proportional to the probability of channels currently being in the open state, with a rate constant, α_b which we call 'rate of unblocking'; such probability is a function of the membrane voltage given by, $br_\infty(V)$, defined as below:

$$br_\infty(V) = \frac{1}{1 + e^{\left((V+40)/12\right)}}$$

The term $(1-br_\infty(V))$, models the steady-state voltage-dependency guiding the unblocking process. The channels being in open state is represented by the term, $(1-b_r)$. Note that if $(1-b_r)$

is close to 1, this means that larger proportion of channels are in an open state, and therefore b_r grows faster, promoting blocking. We modeled $br_\infty(V)$ as a decreasing sigmoid function, such that, at negative membrane potentials, channels have a high probability to enter future depolarized states and therefore, $(1-b_r)\sim 0$, in turn, b_r does not grow fast.

$\boldsymbol{k_b\beta_{br}(V)b_r}$: In this decay term, we assume that the rate of decay of b_r, is proportional to the probability of channels being in the blocked state, with a constant of proportionality k_b, and, this probability is given by a voltage-dependent function, $\beta_{br}(V)$, defined as below:

$$\beta_{br}(V) = \frac{2}{1 + e^{\left(-(V-40)/8\right)}}$$

Note that, $\beta_{br}(V)$ gives a high probability at depolarized potentials, indicating a blocked state and enables decrease in b_r in subsequent time steps.

Taken together, b_r, represents a phenomenological implementation of a previously described block/unblock mechanism of a cytoplasmic blocking particle [19] (see schematic of channel gating in **Fig 3A**). Additionally, a hypothetical competing inactivation variable, h_r, sculpts the voltage-dependent rise and decay times and peak amplitude of sodium resurgence at -40 mV following a brief depolarization (i.e., transient activation), as observed in voltage-clamp experiments (see **Fig 3B**). The functions, $\alpha_{hr}(V),\beta_{hr}(V)$ and $hr_\infty(V)$ are defined as voltage-dependent rate equations that guide the voltage-dependent kinetics and activation/inactivation of the I_{NaR} component as given below.

The steady-state voltage-dependency of the competing inactivation necessary to generate a *resurgent* Na$^+$ current is defined as follows:

$$hr_\infty(V) = \frac{1}{1 + e^{\left((V+40)/20\right)}}$$

The voltage-dependent rate functions of such inactivation is defined by two functions as follows:

$$\alpha_{hr}(V) = \frac{1}{1 + e^{\left(-(V+40)/8\right)}}; \quad \beta_{hr}(V) = \frac{0.5}{1 + e^{\left(-(V+40)/15\right)}}$$

The steepness of the voltage-dependent sigmoid functions for activation and inactivation were tuned to obtain the experimentally observed I_{NaR} activation (see **Fig 3**; also see [11, 14, 30]). To obtain the kinetics (rise and decay times) of I_{NaR} comparable to those observed during voltage-clamp experiments (see **S3 Fig**), the model required three units for the blocking variable (($1-b_r)^3$) and five units for the inactivation variable (h_r^5) (see I_{NaR} equation). Together, the modeled I_{Na} reproduced the key contingencies of the Nav1.6 sodium currents (see **S2 Fig**) [18, 30, 50].

Sensitivity analyses was conducted for the key parameters of I_{NaR} gating including α_b, and, k_b. Note that these two parameters control the rate of blocking. As expected, increasing α_b, that controls rate of increase in b_r, decreased the peak amplitude of I_{NaR}, similar to an experimental increase in block efficacy by a β-peptide (e.g., [19]). On the other hand, k_b also moderates b_r, and increasing k_b, enhances b_r decay rate, that significantly enhanced I_{NaR}, and, therefore burst duration (not shown). Large increases in k_b significantly enhanced I_{NaR}, and indeed transformed bursting to high frequency tonic spiking. However, the effects of I_{NaR} on bursting described in the results section were robust for a wide range of values of these parameters (>100% increase from default values), and, for our simulations, the range of values, $\alpha_b = 0.08$ *to* 0.1, $k_b = 0.8$ *to* 1.2, were used to reproduce Mes V neuron discharge properties. To

reproduce experimentally observed spike width, we additionally tuned the inactivation time constant, $\tau_t = 1.5\pm0.5$, for I_{NaT}.

Potassium and leak currents

The 4-AP sensitive delayed-rectifier type potassium current, I_K, and the leak current, I_{leak} were modeled similar to [8] as below; also see [48].

$$I_K = g_K n(V - E_K)$$

$$I_{leak} = g_{leak}(V - E_{leak})$$

where, the steady-state voltage-dependent activation function for the gating variable, n is given as:

$$n_\infty(V) = \frac{1}{1 + e^{\left(-(V-43)/3.9\right)}}$$

E_K and E_{leak} are K^+ and leak reversal potentials respectively. Model parameter values used are provided in **S1 Table**.

Brain slice preparation

All animal experiments were performed in accordance to the institutional guidelines and regulations using protocols approved by Animal Research Committee at UCLA. Experiments were performed in P8-P14 wild-type mice of either sex. Mice were anesthetized by inhalation of isofluorane and then decapitated. The brainstem was extracted and immersed in ice-cold cutting solution. The brain-cutting solution used during slice preparation was composed of the following (in mM): 194 Sucrose, 30 NaCl, 4.5 KCl, 1.2 NaH_2PO_4, 26 $NaHCO_3$, 10 glucose, 1 $MgCl_2$. The extracted brain block was mounted on a vibrating slicer (DSK Microslicer, Ted Pella) supported by an agar block. Coronal brainstem sections consisting of rostro-caudal extent of Mes V nucleus, spanning midbrain and pons were obtained for subsequent electrophysiological recording.

Voltage-clamp electrophysiology

To obtain direct experimental data to drive I_{NaR} model development, we performed voltage-clamp experiments on Mes V neurons and recorded Na^+ currents by blocking voltage-gated K^+ and Ca^{2+} currents similar to [11]. The pipette internal solution contained the following composition (in mM): 130 CsF, 9 NaCl, 10 HEPES, 10 EGTA, 1 $MgCl_2$, 3 K_2-ATP, and 1 Na-GTP. The external recording solution contained the following composition (in mM): 131 NaCl, 10 HEPES, 3 KCl, 10 glucose, 2 $CaCl_2$, 2 $MgCl_2$, 10 tetraethylammonium (TEA)-Cl, 10 CsCl, 1 4-aminopyridine (4-AP), and 0.3 $CdCl_2$. The voltage-clamp protocol consisted of a holding potential of -90 mV followed by a brief voltage pulse (3 ms) of +30 mV, to remove voltage-dependent block, followed by voltage steps between -70 mV to -10 mV, in steps of 10 mV for ~ 100 ms to activate I_{NaR}, and then returned to -90 mV. A 1 μM TTX abolished the Na^+ current and the residual leak current was subtracted to isolate evident sodium currents. Recordings with series resistance $R_{series} > 0.1R_m$ were discarded, where R_m is the input resistance of the neuron; we did not apply any series resistance compensation.

Dynamic-clamp electrophysiology

Dynamic-clamp electrophysiology and *in vitro* current-clamp recording were used for testing the physiological effects of Na$^+$ currents on burst discharge as well as noise-mediated entropy changes corrected by I_{NaR} [51]. We selected neurons responding with a bursting pattern in response to supra-threshold step current injection in the Mes V nucleus in brainstem slice preparation for our study; >50% of neurons showing other patterns (e.g., tonic or single spiking cells) were discarded. Dynamic-clamp was successfully performed in bursting cells (n = 10). For dynamic-clamp recording, slices were placed in normal ACSF at room temperature (22–25˚C). The ACSF recording solution during patch-clamp recording consisted of the following (in mM): 124 NaCl, 4.5 KCl, 1.2 NaH$_2$PO$_4$, 26 NaHCO$_3$, 10 glucose, 2 CaCl$_2$, 1 MgCl$_2$. Cutting and recording solutions were bubbled with carbogen (95% O$_2$, 5% CO$_2$) and maintained at pH between 7.25–7.3. The pipette internal solution used in current clamp experiments was composed of the following (in mM): 135 K-gluconate, 5 KCl, 0.5 CaCl$_2$, 5 HEPES (base), 5 EGTA, 2 Mg-ATP, and 0.3 Na-ATP with a pH between 7.28–7.3, and osmolarity between 290 ± 5 mOsm. Patch pipettes (3–5 MΩ) were pulled using a Brown/Flaming P-97 micro pipette puller (Sutter Instruments). Slices were perfused with oxygenated recording solution (~2ml/min) at room temperature while secured in a glass bottom recording chamber mounted on an inverted microscope with differential interface contrast optics (Zeiss Axiovert 10). Current clamp (and dynamic-clamp) data were acquired and analyzed using custom-made software (G-Patch, Analysis) with sampling frequency: 10 kHz; cut-off filter frequency: 2 kHz.

The Linux-based Real-Time eXperimental Interface (RTXI v1.3) was used to implement dynamic-clamp, running on a modified Linux kernel extended with the Real-Time Applications Interface, which allows high-frequency, periodic, real-time calculations [52]. The RTXI computer interfaced with the electrophysiological amplifier (Axon Instruments Axopatch 200A, in current-clamp mode) and the data acquisition PC, via a National Instruments PCIe-6251 board. Euler's method with step size 0.05 ms was used for model integration resulting in a computation frequency of 20 kHz.

The model I_{NaR} current used for dynamic clamping into Mes V neuron *in vitro* was developed as discussed above. The ionic conductance g_{NaR} was set to suitable values to introduce model I_{NaR} current into a Mes V neuron during whole-cell current-clamp recording. For dynamic-clamp experiments involving g_{NaR} mediated noise modulation, two approaches were used to model random noise I_{noise}, generated in RTXI and injected as pA current:

1. Uniform-distributed random values (white noise):

$$I_{noise}(t) = (U(t) - 0.5) \cdot A$$

   where $U(t)$ was a uniformly-distributed random number between 0 and 1 generated by the C^{++} *rand()* function, and A was a scaling factor, in this case determining peak-to-peak noise amplitude. It was varied between 3 and 5, to adjust noise amplitudes to produce discernable burst irregularities. The mean injected noise was 0 pA, and its effective standard deviation varied between 0.87 pA ($A = 3$) and 1.44 pA ($A = 5$).

2. Normally distributed random values (Wiener noise).

$$I_{noise}(t) = I_{noise}(t-1) + N(t) \cdot \sqrt{T} \cdot A$$

   where t indicates the value generated at the current computation cycle, and $t-1$ to the value of the previous computation cycle. T was the computation period in seconds (0.00005 s for

20 kHz computation) and was discretized to mimic a Wiener process (random-walk); A was a scaling factor, in this case affecting the noise increment each computation cycle, varying between 3 and 5. $N(t)$ was a normally-distributed random number with mean, $\mu = 0$, and standard deviation, $\sigma = 1$, $N(t)$ was generated from C^{++}-generated uniformly-distributed random numbers using the central limiting theorem:

$$N(t) = \left(\sum_{j=1}^{12} U_j \right) - 6$$

where each U_j is a uniformly-distributed random number between 0 and 1 generated using the C^{++} *rand()* function. In three 1-second simulations, this noise had mean −0.31±0.19 pA ($A = 3$), −0.21±0.62 pA ($A = 4$) or −0.59±0.33 pA ($A = 5$); and standard deviation 0.77±0.13 pA ($A = 3$), 1.07±0.15 pA ($A = 4$) or 1.68±0.44 pA ($A = 5$).

We used stochastic current injection as an external input (additive noise) in order to produce irregularities/uncertainties in burst discharge. Our choice of the noise model was to experimentally disrupt spike timing regularity [45] and is not directly based on any known noise characteristics in Mes V neurons. The jaw muscle spindle afferent Mes V neurons are not known to have spontaneous synaptic events and we did not characterize Na$^+$ channel fluctuations in these neurons [53]. Nonetheless, the stochastic noise we used as shown in the representative example in **Fig 8** most closely matched a diffusive synaptic noise model with Gaussian distribution [54]; **Fig 8C** illustrates the temporal features of the noise inputs described above. A Gaussian white noise generated in MATLAB with zero mean and unit standard deviation or a Wiener noise generated in XPPAUT were used to disrupt firing patterns in the model neuron.

Model simulation and Data analyses

Model simulation and all the analyses were performed using MATLAB (Mathworks) Model code available up on request. Model bifurcation analyses were performed using XPPAUT/AUTO [55]. A variable step Runge-Kutta method 'ode45' was used for current-clamp simulations and 'ode23s' was used for voltage-clamp simulations.

Inter-event intervals (IEI) between spikes in dynamic-clamp recordings were detected using Clampfit 9.0 software and were classified *post hoc* as ISIs and IBIs based on a bi-modal distribution of IEIs. Typically, IEI values < 40 ms were considered as ISIs within bursts and IEI values ≥ 40 ms were considered as IBIs. Any occasional isolated spikes were eliminated from analyses for burst duration calculations.

To calculate Shannons' entropy [56] in the inter-event intervals (IEIs), we generated histograms IEI and calculated the probabilities for each bin of the underlying IEI distributions for each 10 sec spike trains. The probability of kth IEI bin from a distribution of n equal size bins was calculated from the bin counts, $N(k)$ as:

$$p(k) = \frac{N(k)}{\sum_{k=1}^{n} N(k)}$$

The entropy, H was calculated using the following formula:

$$H = - \sum_{k=1}^{n} p_k \log_2 p_k$$

where, n is the total number of IEI bins, each with probability, p_k.

The coefficient of variation (CV) in IEIs was calculated as follows:

$$CV = \frac{s}{\bar{x}}$$

where, s is the IEI sample standard deviation, and, $\bar{x}$ is the sample mean.

Supporting information

S1 Table. Common model parameters used for various simulations presented.
(TIF)

S2 Table. Statistical summary of burst analysis for dynamic-clamp application of resurgent (g_{NaR}) and persistent (g_{NaP}) Na+ conductances/currents.
(TIF)

S1 Fig. a) A state-based Markov model for I_{Na} as in Raman & Bean (2001). C1 to C5 represent sequential closed states and O denotes the open state. I1 through I6 represent the inactivation states for the normal inactivation mechanism. The rate constants in ms^{-1} are: $\alpha = 190e^{(V/20)}$, $\beta = 1.6e^{(-V/19.5)}$, $\gamma = 190$, and, $\delta = 41$. The normal inactivation is voltage-independent and occurs with rate constants, $C_{on} = 0.002$ ms^{-1}, $C_{off} = 0.53$ ms^{-1}, while the O_{on} and O_{off} are 0.2 and 0.003 ms^{-1} respectively. The binding factor 'a' for the inactivating particle is given by $(C_{off}/C_{on})/(O_{off}/O_{on}))^{1/8}$. The rate constant $\varepsilon = 1.75$ ms^{-1}, is the rate at which the open channel block occurs and the exit from the blocked state is modeled as a voltage-dependent process given by $\zeta = 0.03e^{4/67}$ ms^{-1}. **b)** Voltage-clamp simulation of the Markov model shows the resurgent sodium current; Protocol is shown in the inset; Also highlighted are the transient and persistent components. **c)** The sodium current generated during action potentials both in our three-component Hodgkin-Huxley (3HH) type model and the Markov model are shown for comparison; spikes are in blue and sodium current is in red.
(TIF)

S2 Fig. a) Model simulation of sodium channel recovery and its relationship with resurgent current flow. Upper traces in **(a)** and **(b)** show two voltage-clamp protocols with voltages as shown; Δt represents variable intervals from 3–39 ms for the test voltage of -40 mV; lower traces show the corresponding current responses. **c)** Percent channel availability calculated as the peak current at the test steps to -40 mV, normalized to the peak current at the reference pulse of 0 mV; **d)** Steady-state availability, calculated as peak current evoked at 0 mV following a 200 ms pre-pulse conditioning steps (-90 to +30 mV), normalized by the peak current at 0 mV following conditioning at -90 mV.
(TIF)

S3 Fig. a) Rise and decay kinetics in the model (magenta) and experimental trace (black) at a test potential of -40 mV where maximum resurgent current is seen. **b, c)** Rise and decay times for the model and experiments (n = 5) are shown for three test potentials at which a sizable current was seen in $\geq$ 50% of the time; Rise time was calculated from 10–90% of the peak value, and, decay time was calculated from 90–10% of steady-state value at the end of the test pulse. Error bars indicate standard deviation.
(TIF)

S4 Fig. a, c) Representative burst discharge showing the effects of dynamic-clamp subtraction of g_{NaR} **(a)** and g_{NaP} **(c)**; decreasing values of 0.25 and 0.5 nS/pF, and 0.05 and 0.1 nS/pF were used for 1X and 2X g_{NaR} and g_{NaP} respectively. Red double arrows highlight inter-burst intervals (IBIs). The magenta rectangles and the corresponding numbers are shown in expanded

time and voltage in the boxed inset to highlight abolition of STO due to g_{NaP} subtraction (compare upper and middle traces in the box), which was further comparable to setting $g_{NaP} = 0$ in neuron model simulations (lower trace). **a, c)** Box plots showing effects of g_{NaR} **(b)** and g_{NaP} **(d)** subtraction on inter-spike intervals (ISIs) within bursts; C is control. A one-way ANOVA for treatment effect on ISIs had a $p < 0.001$ for g_{NaR} subtraction, with no significant effect of g_{NaP} between C and -1x; however, all spikes were abolished upon -2x g_{NaP} application. Asterisks in **(b)** indicate statistical significance with $p < 0.001$ using a Student t-test for group comparisons (Control v/s -1x and -1x v/s -2x).
(TIF)

S1 Text. Bifurcation analysis of model behavior.
(DOCX)

Acknowledgments

Author Contributions

Conceptualization: Sharmila Venugopal.

Data curation: Sharmila Venugopal.

Formal analysis: Sharmila Venugopal, David H. Terman.

Funding acquisition: Sharmila Venugopal.

Investigation: Sharmila Venugopal, Soju Seki, David H. Terman, Scott H. Chandler.

Methodology: Soju Seki, David H. Terman, Antonios Pantazis.

Project administration: Sharmila Venugopal.

Resources: Riccardo Olcese, Martina Wiedau-Pazos, Scott H. Chandler.

Software: Sharmila Venugopal.

Supervision: Sharmila Venugopal, Riccardo Olcese, Scott H. Chandler.

Visualization: Sharmila Venugopal, Soju Seki.

Writing – original draft: Sharmila Venugopal.

Writing – review & editing: David H. Terman, Antonios Pantazis, Scott H. Chandler.

References

1. Krahe R. & Gabbiani F. Burst firing in sensory systems. *Nat Rev Neurosci* 5, 13–23 (2004). https://doi.org/10.1038/nrn1296 PMID: 14661065

2. Ermentrout B.G. & Terman D.H. Bursting Oscillations. in *Mathematical Foundations of Neuroscience* 103–127 (Springer-Verlag New York, 2010).

3. Del Negro C.A., Hsiao C.F., Chandler S.H. & Garfinkel A. Evidence for a novel bursting mechanism in rodent trigeminal neurons. *Biophys J* 75, 174–182 (1998). https://doi.org/10.1016/S0006-3495(98)77504-6 PMID: 9649377

4. Bialek W., Rieke F., de Ruyter van Steveninck R.R. & Warland D. Reading a neural code. *Science* 252, 1854–1857 (1991). https://doi.org/10.1126/science.2063199 PMID: 2063199

5. Hodgkin A.L. & Huxley A.F. A quantitative description of membrane current and its application to conduction and excitation in nerve. *J Physiol* 117, 500–544 (1952). https://doi.org/10.1113/jphysiol.1952.sp004764 PMID: 12991237

6. Catterall W.A. From ionic currents to molecular mechanisms: the structure and function of voltage-gated sodium channels. *Neuron* 26, 13–25 (2000). PMID: 10798388

7. Alonso A. & Llinás R.R. Subthreshold Na+-dependent theta-like rhythmicity in stellate cells of entorhinal cortex layer II. *Nature* 342, 175–177 (1989). https://doi.org/10.1038/342175a0 PMID: 2812013

8. Wu N., et al. Persistent sodium currents in mesencephalic v neurons participate in burst generation and control of membrane excitability. *J Neurophysiol* 93, 2710–2722 (2005). https://doi.org/10.1152/jn.00636.2004 PMID: 15625100

9. Hutcheon B. & Yarom Y. Resonance, oscillation and the intrinsic frequency preferences of neurons. *Trends Neurosci* 23, 216–222 (2000). PMID: 10782127

10. Schwindt P.C. & Crill W.E. Amplification of synaptic current by persistent sodium conductance in apical dendrite of neocortical neurons. *J Neurophysiol* 74, 2220–2224 (1995). https://doi.org/10.1152/jn.1995.74.5.2220 PMID: 8592214

11. Enomoto A., Han J.M., Hsiao C.F., Wu N. & Chandler S.H. Participation of sodium currents in burst generation and control of membrane excitability in mesencephalic trigeminal neurons. *J Neurosci* 26, 3412–3422 (2006). https://doi.org/10.1523/JNEUROSCI.5274-05.2006 PMID: 16571748

12. Del Negro C.A., Koshiya N., Butera R.J. & Smith J.C. Persistent sodium current, membrane properties and bursting behavior of pre-bötzinger complex inspiratory neurons in vitro. *J Neurophysiol* 88, 2242–2250 (2002). https://doi.org/10.1152/jn.00081.2002 PMID: 12424266

13. Yamanishi T., Koizumi H., Navarro M.A., Milescu L.S. & Smith J.C. Kinetic properties of persistent Na. *J Gen Physiol* 150, 1523–1540 (2018). https://doi.org/10.1085/jgp.201812100 PMID: 30301870

14. Enomoto A., Han J.M., Hsiao C.F. & Chandler S.H. Sodium currents in mesencephalic trigeminal neurons from Nav1.6 null mice. *J Neurophysiol* 98, 710–719 (2007). https://doi.org/10.1152/jn.00292.2007 PMID: 17522178

15. Afshari F.S., et al. Resurgent Na currents in four classes of neurons of the cerebellum. *J Neurophysiol* 92, 2831–2843 (2004). https://doi.org/10.1152/jn.00261.2004 PMID: 15212420

16. Khaliq Z.M. & Raman I.M. Relative contributions of axonal and somatic Na channels to action potential initiation in cerebellar Purkinje neurons. *J Neurosci* 26, 1935–1944 (2006). https://doi.org/10.1523/JNEUROSCI.4664-05.2006 PMID: 16481425

17. Raman I.M. & Bean B.P. Properties of sodium currents and action potential firing in isolated cerebellar Purkinje neurons. *Ann N Y Acad Sci* 868, 93–96 (1999). https://doi.org/10.1111/j.1749-6632.1999.tb11279.x PMID: 10414287

18. Raman I.M. & Bean B.P. Resurgent sodium current and action potential formation in dissociated cerebellar Purkinje neurons. *J Neurosci* 17, 4517–4526 (1997). PMID: 9169512

19. Grieco T.M., Malhotra J.D., Chen C., Isom L.L. & Raman I.M. Open-channel block by the cytoplasmic tail of sodium channel beta4 as a mechanism for resurgent sodium current. *Neuron* 45, 233–244 (2005). https://doi.org/10.1016/j.neuron.2004.12.035 PMID: 15664175

20. Raman I.M., Sprunger L.K., Meisler M.H. & Bean B.P. Altered subthreshold sodium currents and disrupted firing patterns in Purkinje neurons of Scn8a mutant mice. *Neuron* 19, 881–891 (1997). PMID: 9354334

21. Magistretti J., Castelli L., Forti L. & D'Angelo E. Kinetic and functional analysis of transient, persistent and resurgent sodium currents in rat cerebellar granule cells in situ: an electrophysiological and modelling study. *J Physiol* 573, 83–106 (2006). https://doi.org/10.1113/jphysiol.2006.106682 PMID: 16527854

22. Kim J.H., Kushmerick C. & von Gersdorff H. Presynaptic resurgent Na+ currents sculpt the action potential waveform and increase firing reliability at a CNS nerve terminal. *J Neurosci* 30, 15479–15490 (2010). https://doi.org/10.1523/JNEUROSCI.3982-10.2010 PMID: 21084604

23. Ransdell J.L., et al. Loss of Navβ4-Mediated Regulation of Sodium Currents in Adult Purkinje Neurons Disrupts Firing and Impairs Motor Coordination and Balance. *Cell Rep* 19, 532–544 (2017). https://doi.org/10.1016/j.celrep.2017.03.068 PMID: 28423317

24. Browne L., Smith K.E. & Jagger D.J. Identification of Persistent and Resurgent Sodium Currents in Spiral Ganglion Neurons Cultured from the Mouse Cochlea. *eNeuro* 4 (2017).

25. Levin S.I., et al. Impaired motor function in mice with cell-specific knockout of sodium channel Scn8a (NaV1.6) in cerebellar purkinje neurons and granule cells. *J Neurophysiol* 96, 785–793 (2006). https://doi.org/10.1152/jn.01193.2005 PMID: 16687615

26. Seki S., et al. Pre-symptomatic abnormalities and associated channelopathies in spindle afferent trigeminal mesencephalic V neurons in a SOD1G93A mouse model for Amyotrophic Lateral Sclerosis. in *Society for Neuroscience* 2017 (Washington D.C., 2017).

27. Amir R., Michaelis M. & Devor M. Burst discharge in primary sensory neurons: triggered by subthreshold oscillations, maintained by depolarizing afterpotentials. *J Neurosci* 22, 1187–1198 (2002). PMID: 11826148

28. Ottolini M., Barker B.S., Gaykema R.P., Meisler M.H. & Patel M.K. Aberrant sodium channel currents and hyperexcitability of medial entorhinal cortex neurons in a mouse model of SCN8A encephalopathy. *J Neurosci* (2017).

29. Jarecki B.W., Piekarz A.D., Jackson J.O. & Cummins T.R. Human voltage-gated sodium channel mutations that cause inherited neuronal and muscle channelopathies increase resurgent sodium currents. *J Clin Invest* 120, 369–378 (2010). https://doi.org/10.1172/JCI40801 PMID: 20038812

30. Raman I.M. & Bean B.P. Inactivation and recovery of sodium currents in cerebellar Purkinje neurons: evidence for two mechanisms. *Biophys J* 80, 729–737 (2001). https://doi.org/10.1016/S0006-3495(01)76052-3 PMID: 11159440

31. Balbi P., Massobrio P. & Hellgren Kotaleski J. A single Markov-type kinetic model accounting for the macroscopic currents of all human voltage-gated sodium channel isoforms. *PLoS Comput Biol* 13, e1005737 (2017). https://doi.org/10.1371/journal.pcbi.1005737 PMID: 28863150

32. Milescu L.S., Yamanishi T., Ptak K., Mogri M.Z. & Smith J.C. Real-time kinetic modeling of voltage-gated ion channels using dynamic clamp. *Biophys J* 95, 66–87 (2008). https://doi.org/10.1529/biophysj.107.118190 PMID: 18375511

33. Milescu L.S., Yamanishi T., Ptak K. & Smith J.C. Kinetic properties and functional dynamics of sodium channels during repetitive spiking in a slow pacemaker neuron. *J Neurosci* 30, 12113–12127 (2010). https://doi.org/10.1523/JNEUROSCI.0445-10.2010 PMID: 20826674

34. Enomoto A., et al. Development of resurgent and persistent sodium currents in mesencephalic trigeminal neurons. *J Neurosci Res* (2017).

35. Wu N., Hsiao C.F. & Chandler S.H. Membrane resonance and subthreshold membrane oscillations in mesencephalic V neurons: participants in burst generation. *J Neurosci* 21, 3729–3739 (2001). PMID: 11356860

36. Yang J., et al. Membrane current-based mechanisms for excitability transitions in neurons of the rat mesencephalic trigeminal nuclei. *Neuroscience* 163, 799–810 (2009). https://doi.org/10.1016/j.neuroscience.2009.07.007 PMID: 19591906

37. Khaliq Z.M., Gouwens N.W. & Raman I.M. The contribution of resurgent sodium current to high-frequency firing in Purkinje neurons: an experimental and modeling study. *J Neurosci* 23, 4899–4912 (2003). PMID: 12832512

38. Birmingham J.T., Szuts Z.B., Abbott L.F. & Marder E. Encoding of muscle movement on two time scales by a sensory neuron that switches between spiking and bursting modes. *J Neurophysiol* 82, 2786–2797 (1999). https://doi.org/10.1152/jn.1999.82.5.2786 PMID: 10561445

39. Zheng Y. & Escabí M.A. Proportional spike-timing precision and firing reliability underlie efficient temporal processing of periodicity and envelope shape cues. *J Neurophysiol* 110, 587–606 (2013). https://doi.org/10.1152/jn.01080.2010 PMID: 23636724

40. Reich D.S., Mechler F., Purpura K.P. & Victor J.D. Interspike intervals, receptive fields, and information encoding in primary visual cortex. *J Neurosci* 20, 1964–1974 (2000). PMID: 10684897

41. Tiesinga P., Fellous J.M. & Sejnowski T.J. Regulation of spike timing in visual cortical circuits. *Nat Rev Neurosci* 9, 97–107 (2008). https://doi.org/10.1038/nrn2315 PMID: 18200026

42. Mainen Z.F. & Sejnowski T.J. Reliability of spike timing in neocortical neurons. *Science* 268, 1503–1506 (1995). https://doi.org/10.1126/science.7770778 PMID: 7770778

43. Vilin Y.Y. & Ruben P.C. Slow inactivation in voltage-gated sodium channels: molecular substrates and contributions to channelopathies. *Cell Biochem Biophys* 35, 171–190 (2001). https://doi.org/10.1385/CBB:35:2:171 PMID: 11892790

44. Béhuret S., Deleuze C. & Bal T. Corticothalamic Synaptic Noise as a Mechanism for Selective Attention in Thalamic Neurons. *Front Neural Circuits* 9, 80 (2015). https://doi.org/10.3389/fncir.2015.00080 PMID: 26733818

45. Faisal A.A., Selen L.P. & Wolpert D.M. Noise in the nervous system. *Nat Rev Neurosci* 9, 292–303 (2008). https://doi.org/10.1038/nrn2258 PMID: 18319728

46. Izhikevich E.M., Desai N.S., Walcott E.C. & Hoppensteadt F.C. Bursts as a unit of neural information: selective communication via resonance. *Trends Neurosci* 26, 161–167 (2003). https://doi.org/10.1016/S0166-2236(03)00034-1 PMID: 12591219

47. Lisman J.E. Bursts as a unit of neural information: making unreliable synapses reliable. *Trends Neurosci* 20, 38–43 (1997). https://doi.org/10.1016/S0166-2236(96)10070-9 PMID: 9004418

48. Del Negro C.A. & Chandler S.H. Physiological and theoretical analysis of K+ currents controlling discharge in neonatal rat mesencephalic trigeminal neurons. *J Neurophysiol* 77, 537–553 (1997). https://doi.org/10.1152/jn.1997.77.2.537 PMID: 9065827

49. Taddese A. & Bean B.P. Subthreshold sodium current from rapidly inactivating sodium channels drives spontaneous firing of tuberomammillary neurons. *Neuron* 33, 587–600 (2002). PMID: 11856532

50. Smith M.R., Smith R.D., Plummer N.W., Meisler M.H. & Goldin A.L. Functional analysis of the mouse Scn8a sodium channel. *J Neurosci* 18, 6093–6102 (1998). PMID: 9698304

51. Prinz A.A., Abbott L.F. & Marder E. The dynamic clamp comes of age. *Trends Neurosci* 27, 218–224 (2004). https://doi.org/10.1016/j.tins.2004.02.004 PMID: 15046881

52. Lin R.J., Bettencourt J., Wha Ite J., Christini D.J. & Butera R.J. Real-time experiment interface for biological control applications. *Conf Proc IEEE Eng Med Biol Soc* 2010, 4160–4163 (2010). https://doi.org/10.1109/IEMBS.2010.5627397 PMID: 21096883

53. Verdier D., Lund J.P. & Kolta A. Synaptic inputs to trigeminal primary afferent neurons cause firing and modulate intrinsic oscillatory activity. *J Neurophysiol* 92, 2444–2455 (2004). https://doi.org/10.1152/jn.00279.2004 PMID: 15381749

54. Fourcaud-Trocmé N., Hansel D., van Vreeswijk C. & Brunel N. How spike generation mechanisms determine the neuronal response to fluctuating inputs. *J Neurosci* 23, 11628–11640 (2003). PMID: 14684865

55. Ermentrout B. XPPAUT5.0 –the differential equations tool. (2001).

56. Shannon C.E. & Weaver W. *The Mathematical Theory of Communication* (University of Illinois Press, Urbana, 1949).